UNIVERSITY OF CALIFORNIA,
IRVINE

A Study of BER, EVM, and OOBE Degradation in Transceivers Incorporating Digital Modulation Schemes Due to Noise and Non-Linearity

THESIS

submitted in partial satisfaction of the requirements
for the degree of

MASTER OF SCIENCE

in Electrical and Computer Engineering

by

Mohammad Oveisi

Thesis Committee:
Chancellor's Professor Payam Heydari, Chair
Distinguished Professor A. Lee Swindlehurst
Assistant Professor Hamidreza Aghasi

2023

DEDICATION

To my family and friends

TABLE OF CONTENTS

LIST OF FIGURES

ACKNOWLEDGMENTS

I am sincerely grateful to all those who have provided unwavering support and guidance throughout the course of completing this thesis. Their invaluable encouragement, wisdom, and assistance have significantly contributed to its realization.

I extend my heartfelt appreciation to my esteemed supervisor, Professor Payam Heydari, for his exceptional guidance, patience, and insightful feedback. His mentorship has been pivotal in shaping the trajectory of this research.

My gratitude also extends to my friends and family for their steadfast support, understanding, and encouragement. Their belief in my capabilities has remained a constant source of motivation.

I am indebted to the University of California, Irvine for providing the essential resources and conducive environment that facilitated the successful completion of this thesis.

Furthermore, I extend heartfelt gratitude to the authors, researchers, and scholars whose foundational work has underpinned this study. Your contributions have been instrumental in refining my understanding of the subject matter. I am also grateful to the co-authors of the papers I have had the privilege to publish.

I would also like to express my profound gratitude to Professor Behzad Razavi. His books in this field have served as an enduring source of inspiration, not only for myself but for a several students globally. The depth of insight and clarity in Professor Razavi's books have been instrumental in shaping my understanding and competence in this subject matter. I extend my sincere acknowledgment to him for his invaluable contributions, which have left an indelible mark on my academic journey and have undoubtedly enriched the knowledge base of countless aspiring scholars worldwide.

In summary, this thesis stands as a testament to the collective contributions of those who have shaped my academic voyage. While it is impossible to individually acknowledge everyone, please recognize that your influence has not gone unnoticed.

Sincerely,

Mohammad Oveisi

VITA

Mohammad Oveisi

EDUCATION

Master of Science in Electrical and Computer Engineering **2023**
University of California, Irvine *Irvine, CA*

Bachelor of Science in Electrical Engineering **2020**
Sharif University of Technology *Tehran, Iran*

RESEARCH EXPERIENCE

Graduate Research Assistant **2021–2023**
University of California, Irvine *Irvine, CA*

Undergraduate Research Assistant **2019–2020**
Sharif University of Technology *Tehran, Iran*

TEACHING EXPERIENCE

Undergraduate Teaching Assistant **2017–2020**
Sharif University of Technology *Tehran, Iran*

REFEREED JOURNAL PUBLICATIONS

A Study of Out-of-Band Emission in Digital Transmitters Due to PLL Phase Noise, Circuit Non-Linearity, and Bandwidth Limitation **2023**
IEEE Open Journal of Circuits and Systems

A Study of a Millimeter-Wave Transmitter Architecture Realizing QAM Directly in RF Domain **2023**
IEEE Transactions on Circuits and Systems I: Regular Papers

A Study of BER and EVM Degradation in Digital Modulation Schemes Due to PLL Jitter and Communication-Link Noise **2022**
IEEE Transactions on Circuits and Systems I: Regular Papers

REFEREED CONFERENCE PUBLICATIONS

A Comparative Study of RF-QAM and Conventional Transmitter Architectures **May 2023**
IEEE International Symposium on Circuits and Systems

ABSTRACT OF THE THESIS

A Study of BER, EVM, and OOBE Degradation in Transceivers Incorporating Digital Modulation Schemes Due to Noise and Non-Linearity

By

Mohammad Oveisi

Master of Science in Electrical and Computer Engineering

University of California, Irvine, 2023

Chancellor's Professor Payam Heydari, Chair

The phase-locked-based frequency synthesizer, essential in wireless transceivers (TRXs), introduces phase noise and jitter, undermining digital communication link performance. This thesis analyzes the impact of the communication-link noise, phase-locked loop (PLL) phase noise, and circuit non-linearity on TRX's key parameters such as out-of-band emission (OOBE), error-vector magnitude (EVM), and bit-error-rate (BER) for prevalent digital modulation schemes. Phase noise and jitter characteristics for generic integer-N and fractional-N PLLs, as a local oscillator (LO) for an RF mixer, are derived, while accounting for reference spurs, mixer cyclo-stationarity, and additive noise in communication links. Utilizing a comprehensive jitter model and detailed circuit non-linearity model, their impact on digital modulation schemes is investigated. Analyzing M-ary phase-shift keying (M-PSK) and 4^M quadrature amplitude modulation (4^MQAM), the resulting degradation in key metrics is evaluated. The developed analytical models' accuracy is confirmed through meticulous comparison with system-level simulations, affirming their reliability. In essence, this thesis presents a comprehensive exploration of the system's non-idealities on a generic transceiver's performance. Additionally, this research advances the designers' understanding and equips them with valuable insights crucial for optimizing the performance of wireless transceivers in the presence of inevitable non-idealities.

Chapter 1

Introduction

Digital modulation/demodulation is the core processing task in all modern wireless transceivers. Increasing the modulation order enhances spectral efficiency, which, in turn, helps accommodate user demand for higher data rate without the need to proportionally increase the bandwidth [1]. Bit-error rate (BER), error-vector-magnitude (EVM), and out-of-band emission (OOBE) are among the most important parameters providing quantitative assessments of performance in a communication link [2, 3]. As a common state of knowledge, BER increases with an increase in modulation order for given symbol signal-to-noise ratio, S_s/N_0, where S_s and N_0 denote the signal symbol and noise powers, respectively. Additionally, EVM provides a measure of how accurately a radio is transmitting symbols within its constellation, while OOBE is a measure of how purely a transmitter (TX) is transmitting the signal in its own specific frequency band while avoiding interference with other transceivers operating in adjacent bands.

1.1 Bit-Error Rate (BER)

At the heart of wireless communication systems lies the fundamental goal of flawlessly transmitting information between two points that are physically separated. Particularly in scenarios involving digital data, such as binary information, an indispensable facet of the transceiver's efficacy is its ability to maintain fidelity in information transfer. Therefore, a crucial aspect of how well a transceiver performs is its ability to ensure accuracy during the transfer of this information. A key factor in this evaluation is the determination of how frequently incorrect bits of data are transferred within a defined set of data. To be more precise, it is of paramount importance to measure the probability that the receiving device obtains a binary "0" (or "1") when the sending module actually intended to transmit a binary "1" (or "0"). This probabilistic measurement, commonly known as BER, serves as a crucial numerical representation of the system's overall performance and reliability. In essence, BER provides insight into how well the wireless communication system (especially the receiver) can maintain the integrity of the data being transferred, indicating the level of confidence one can have in the accuracy of the transmitted information. In general, BER is obtained, as follows

$$BER = \frac{N_W}{N_T} = 1 - \frac{N_C}{N_T} \tag{1.1}$$

where N_T, N_C, and N_W are the number of total, correct, and incorrect received bits, respectively.

1.2 Error-Vector Magnitude (EVM)

In addition to BER, EVM is another significant metric in communication systems to quantify the quality of modulation and demodulation processes. It provides a comprehensive assess-

ment of the accuracy of a transmitted signal when compared to the expected ideal signal. In essence, EVM measures the discrepancy between the actual transmitted signal and the reference signal that represents the ideal, error-free version of the transmitted signal. This discrepancy is typically expressed as a percentage or in decibels.

EVM plays a crucial role in evaluating the performance of wireless communication systems (especially transmitters), particularly in scenarios where various factors like noise, interference, and signal distortion can affect the transmitted signal. By quantifying the difference between the received signal and the ideal signal, EVM offers insights into the distortion, phase errors, and amplitude errors introduced during transmission and reception. High EVM values indicate a greater deviation from the ideal signal and suggest poor signal quality, potentially leading to data corruption or reduced system efficiency. On the other hand, low EVM values indicate that the transmitted signal closely aligns with the desired signal, highlighting a higher degree of accuracy and reliability in the communication process.

1.3 Out-of-Band Emission (OOBE)

interconnected nature of today's world has necessitated the implementation of a multitude of standards for various wireless communication technologies. This has resulted in a densely populated spectrum, with different frequency bands allocated for various applications and numerous channels within each specific band. With the increasing number of devices and technologies vying for the limited frequency band, it has become increasingly challenging to maintain spectral purity and control OOBE. The interference with other communication systems, directly caused by OOBE, results in a degradation of the received-signal quality [4, 5, 6]. Accordingly, significant research efforts have been undertaken to reduce the OOBE power levels associated with different modulation schemes in RF TXs [7, 8, 9, 10, 11]. However, TX designs aiming for OOBE reduction may introduce additional distortions that

increase the system BER, resulting in a trade-off between OOBE and BER [12].

1.4 Communication-Link Noise

Noise, as the main source of link impairment, is caused by several sources including amplitude noise sources (i.e., channel noise and the receiver's input-referred noise) and local oscillator (LO) phase noise and jitter. Thermal noise is a ubiquitous form of noise that emerges in electronic systems due to the random motion of electrons caused by thermal energy [13, 14]. This noise is a fundamental aspect of any electronic device and arises at temperatures above absolute zero. In the context of transceiver performance, thermal noise has a notable impact on signal integrity and overall system functionality [4]. Thermal noise contributes to the degradation of the signal-to-noise ratio (SNR) within a transceiver system. As the transceiver processes electronic signals, the random motion of electrons induced by thermal energy generates small fluctuations in voltage and current levels, effectively adding an unpredictable noise component to the signal. These voltage/current fluctuations can mask the actual signal, making it more difficult for the receiving end to accurately distinguish the transmitted information from the noise. Consequently, as the thermal noise level increases, the SNR decreases, leading to a compromised ability to reliably decode the transmitted data. Careful consideration of the system's noise figure, which characterizes how much additional noise the transceiver itself contributes, is a crucial factor in managing the impact of thermal noise on transceiver performance.

1.5 Phase Noise

The LO phase noise wields more influence on BER and EVM degradation in high-order modulations [15]. The way it impacts the link performance contrasts markedly with amplitude

noise sources at RF frequencies, which are modeled mostly as wideband white stochastic processes. Phase noise, on the other hand, is a non-additive colored process whose power spectral density (PSD) has been carefully investigated in [16, 17, 18]. The impact of PLL jitter on EVM is often considerable in mm-wave LO circuits due to wide channel bandwidths and large phase noise of high frequency voltage-controlled oscillators (VCOs) [19]. The deteriorating effect of phase noise manifests in a random rotation of the signal constellation, leading to an increase in EVM and BER [4, 20]. Phase noise can also destroy the orthogonality of sub-carriers in an orthogonal frequency division multiplexing (OFDM) system [21], and degrade the sum-rate performance of multi-user MIMO systems [22]. These detrimental effects have forced many researchers to use a variety of techniques to reduce the PLL jitter. For example, the digital carrier phase tracking algorithms that run in the back-end, as outlined in [23], reduces the phase noise and jitter significantly.

As was noted in [17, 24], the oscillator phase noise profile is comprised of three regions. A region with a slope of -30 dB/dec denotes the close-in phase-noise variation at low offset frequencies. The profile drops with -20 dB/dec slope further away from the oscillation frequency, which eventually flattens at the far-out frequencies. The close-in phase noise is primarily suppressed by the PLL loop dynamic upon a proper choice of loop bandwidth, while the far-out tail is inconsequential to jitter. Therefore, only the $1/f^2$ region of the oscillator phase noise is often taken into consideration. This explicitly means that the focus of the phase-noise analysis would revolve around transistor's thermal noise sources with white Gaussian PSD, while omitting the flicker noise.

1.6 Nonlinearity

In addition to phase noise, another unavoidable circuit nonideality affecting the performance of TRXs is the nonlinearity of various building blocks. Circuit nonlinearity, which is charac-

terized by 1-dB compression point (P_{1dB}) and n^{th}-order intercept point (IP_n), results in the generation of harmonics and intermodulation products that may extend beyond the intended frequency band[4, 25]. The presence of these harmonics and intermodulation products can generate large in-band blockers due to the circuit nonlinearity, degrading OOBE. Therefore, various filtering stages are used within a TX to control the spectrum of the transmitted signal and to reduce OOBE levels.

Chapter 2

Frequency Synthesizers

Frequency synthesizers play a pivotal role in modern communication systems, enabling devices to generate stable and precise radio frequency signals for a wide range of applications such as wireless communication, radar systems, and satellite communication. Among the various techniques employed for frequency synthesis, the phase-locked loop (PLL) stands out as a versatile and widely used method. PLL-based frequency synthesizers offer the capability to generate stable output frequencies that are controllable and accurately locked to a reference frequency [26]. This feature has been proven to be essential for maintaining signal integrity, spectral purity, and frequency accuracy, which are critical aspects of communication systems requiring coherent and synchronized signals [27].

Two prominent configurations of PLL-based frequency synthesizers are the integer-N and fractional-N synthesizers. The integer-N synthesizer allows the output frequency to be synthesized using a frequency divider with integer division ratios. While it offers simplicity and robust performance for applications demanding discrete frequency steps, it can be limited in terms of achieving precise frequency resolutions, especially when the desired output frequency falls between two integer multiples of the reference frequency. In contrast, the fractional-N

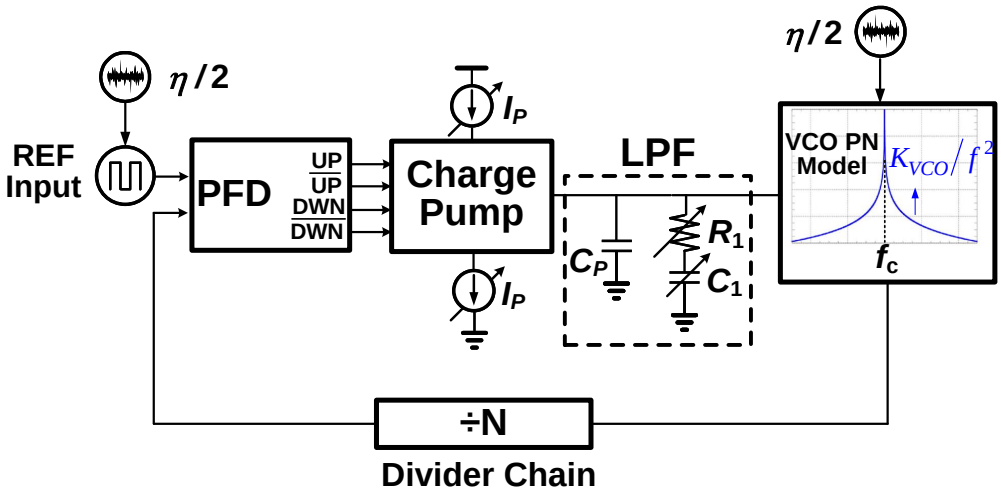

Figure 2.1: The general block diagram of an integer-N PLL.

synthesizer enhances frequency resolution by employing fractional division ratios, enabling the generation of frequencies that lie between the integer divisions. The fractional-N frequency synthesizer is particularly beneficial for applications requiring fine-tuning capabilities and allows for more flexible frequency selection. However, the fractional-N approach introduces challenges related to spurious signals and phase noise due to the fractional division process. Despite their distinct advantages and challenges, both integer-N and fractional-N synthesizers contribute significantly to the field of frequency synthesis.

2.1 Integer-N Frequency Synthesizer

Integer-N frequency synthesizers are commonly used in various transceivers. This section presents the contribution of each noise source to the absolute phase jitter variance at the output of the PLL, as was demonstrated by prior works [26, 28, 29]. Fig. 2.1 shows the block diagram of a conventional integer-N PLL for the phase-noise analysis. As has been extensively shown by prior works [4, 30], two noise sources predominately contribute to the PLL phase noise and timing jitter: (1) VCO phase noise and (2) reference noise. Considering the white Gaussian noise with the PSD of $\eta/2$, as well as the flicker noise, at the VCO input,

the output noise PSD of a free-running VCO is $S_{VCO}(f) = \frac{\alpha}{f^2} + \frac{\gamma}{f^3}$, where K_{VCO} is the VCO gain, and $\alpha = K_{VCO}^2 \times \frac{\eta}{2}$.

Additionally, PLL-based frequency synthesizers for wireless transceivers are often fed by crystal oscillators. A crystal oscillator typically displays a flat phase-noise profile beyond an offset of a few kilohertz[4, 31]. Therefore, the input clock noise is assumed to be white with a PSD of $S_{n,in}(f) = \frac{\eta}{2} \times K_{clk}^2$, where K_{clk} is the reference oscillator's gain. The VCO and input noise sources are shaped by the loop transfer function from the corresponding source to the output. The PLL transfer function due to VCO phase noise is a high pass filter, given by [26]:

$$\frac{\phi_{out}}{\phi_{VCO}}(s) = \frac{s^2}{s^2 + 2\zeta\omega_n s + \omega_n^2} \tag{2.1}$$

where ζ is the damping factor and ω_n is the natural frequency of the PLL [26]:

$$\zeta = \frac{R_1}{2}\sqrt{\frac{I_p C_1}{2\pi}\frac{K_{VCO}}{N}},\ \omega_n = 2\pi f_n = \sqrt{\frac{I_p}{2\pi C_1}\frac{K_{VCO}}{N}} \tag{2.2}$$

where R_1 and C_1 are loop filter's resistor and capacitor, respectively. I_p is the charge pump current, and N is the division ratio between output and input frequencies.

The PLL phase jitter due to the VCO phase noise, omitting the flicker noise contribution, is given by [28],[29]

$$\sigma^2_{\Delta\phi_{VCO}} = \frac{K_{VCO}^2\eta}{4\zeta\omega_n} = \frac{\pi N K_{VCO}\eta}{R_1 I_p} \tag{2.3}$$

As for the input reference contribution, the transfer function from the input noise source to the output is a low pass filter, given by [4]:

$$\frac{\phi_{out}}{\phi_{in}}(s) = N\frac{2\zeta\omega_n s + \omega_n^2}{s^2 + 2\zeta\omega_n s + \omega_n^2} \tag{2.4}$$

The phase jitter variance due to input noise is given by [30],[28]

$$\sigma^2_{\Delta\phi_{in}} = \eta N^2 K^2_{clk}\omega_n \frac{4\zeta^2+1}{4\zeta} = \eta N^2 K^2_{clk}\left(\frac{R_1 I_p K_{VCO}}{4\pi N} + \frac{1}{2R_1 C_1}\right) \tag{2.5}$$

Leveraging the superposition principle, the PLL's phase-noise PSD is derived to be:

$$S_\Phi(f) = \frac{[\alpha + 4\eta N^2\zeta^2 f_n^2]f^2 + \gamma f + \eta N^2 f_n^4}{f^4 + 2(2\zeta^2-1)f_n^2 f^2 + f_n^4} \tag{2.6}$$

Eq. (2.6) at low and high frequencies can be approximated, as follows

$$S_\Phi(f)\Big|_{low\ f} = \eta N^2 \tag{2.7}$$

$$S_\Phi(f)\Big|_{high\ f} = \frac{\alpha + 4\eta N^2\zeta^2 f_n^2}{f^2} \tag{2.8}$$

Therefore, Eq. (2.6) can be well approximated by:

$$S_\Phi(f) = \begin{cases} \eta N^2 & f \le f_1 \\ \eta N^2 \frac{f_1^2}{f^2} & f > f_1 \end{cases} \tag{2.9}$$

where $f_1 = \sqrt{\frac{\alpha}{\eta N^2} + (2\zeta f_n)^2}$. It is seen that if $\alpha \ll 4\eta N^2\zeta^2 f_n^2$, then, $f_1 \approx 2\zeta f_n$, which approximately denotes the PLL loop bandwidth. For example, consider a type-II PLL with $\zeta = 1$, $f_n = 5$ MHz, $N = 280$, and fed by an input clock whose single side-band (SSB) phase noise is -160 dBc/Hz (i.e., $\eta = 5 \times 10^{-17}$). The VCO oscillates at 28 GHz with an SSB phase noise of -107 dBc/Hz at 1 MHz offset and with a phase noise corner frequency of 1 MHz (i.e., $\alpha = 5$ and $\gamma = 5 \times 10^6$). Fig. 2.2 shows plots of Eqs. (2.6) and (2.9) as well as input and VCO phase noise profiles. This plot verifies the accuracy of this approximation.

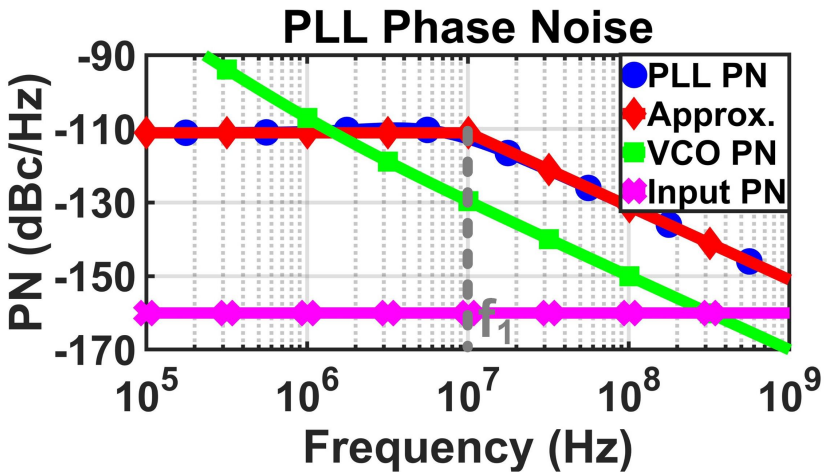

Figure 2.2: PLL phase noise profile and its approximation.

The variance of a stationary process is widely known to be obtained from its PSD, as follows

$$\sigma^2_{\Delta\phi} = \int_{-\infty}^{\infty} S_\phi(f)\, df, \tag{2.10}$$

where $S_\phi(f)$ is the two-sided output phase PSD. It should be noted that integrated OFDM systems often incorporate a phase-noise reduction technique following the down-conversion of the RF signal to the baseband, which is known as common phase-error (CPE) correction. In particular, in OFDM systems, some carriers are used as pilot tones to correct the remaining carriers to remove CPE. This procedure can be modeled by a high-pass filter weighting function applied to the synthesizer phase-noise spectrum [32]. The RMS phase jitter of the OFDM system with sub-carrier spacing of Δf_{sub} after CPE correction is calculated to be [33]:

$$\sigma^2_{\Delta\phi} = 2\int_0^{B/2} S_\phi(f)\,[1 - \mathrm{sinc}^2(fT_u)]df \tag{2.11}$$

where $\mathrm{sinc}(x) = \frac{\sin(\pi x)}{\pi x}$, $T_u = 1/\Delta f_{sub}$, and B denotes the bandwidth of the entire OFDM band. The absolute phase jitter (referenced to a perfect time scale) is related to the phase-

noise PSD using Eq. (2.12) [34]:

$$\sigma_{\Delta\phi} = \sqrt{2 \times \int_{f_1}^{f_2} 10^{\frac{\mathcal{L}(\Delta f)}{10}} df} \tag{2.12}$$

where $\mathcal{L}(\Delta f)$ is the phase-noise PSD in dBc/Hz, and f_1 and f_2 are determined by the jitter mask, specific to an application. Moreover, the phase jitter can also be obtained from PLL parameters.

Assuming the VCO and reference noise are both Gaussian, they will remain Gaussian as they pass through linear filters within the loop. Therefore, the PLL jitter will assume a Gaussian distribution whose variance, $\sigma^2_{\Delta\phi_{PLL}}$, is the sum of phase-jitter variances due to VCO and reference noise. The PLL RMS phase jitter is readily calculated to be:

$$\sigma_{\Delta\phi_{PLL}} = \sqrt{\frac{K^2_{VCO}\eta}{4\zeta\omega_n} + \eta N^2 K^2_{clk}\omega_n \frac{4\zeta^2+1}{4\zeta}} \tag{2.13}$$

The above RMS phase-jitter equation is only applicable to integer-N PLL of Fig. 2.1. Clearly, distinct closed-form expressions should be derived for other types, e.g., an all-digital PLL (AD-PLL).

In practice, to guarantee the loop stability, $\zeta \geqslant 1$. At the same time, $\zeta > 1.5$ results in a large loop acquisition time, rendering the PLL impractical for many applications. On the other hand, K_{VCO} and N are determined by tuning range and output frequency, respectively. Therefore, for a given ζ, K_{VCO}, and N, $\sigma_{\Delta\phi_{PLL}}$ is minimized when $\omega_n = \omega_{n,\text{opt}} = K_{VCO}/[K_{clk}M\sqrt{1+4\zeta^2}]$. The minimum value of $\sigma_{\Delta\phi_{PLL}}$ under this condition equals to:

$$\sigma_{\Delta\phi_{PLL,\min}} = \sqrt{\eta M K_{clk} K_{VCO}\sqrt{1+\frac{1}{4\zeta^2}}} \tag{2.14}$$

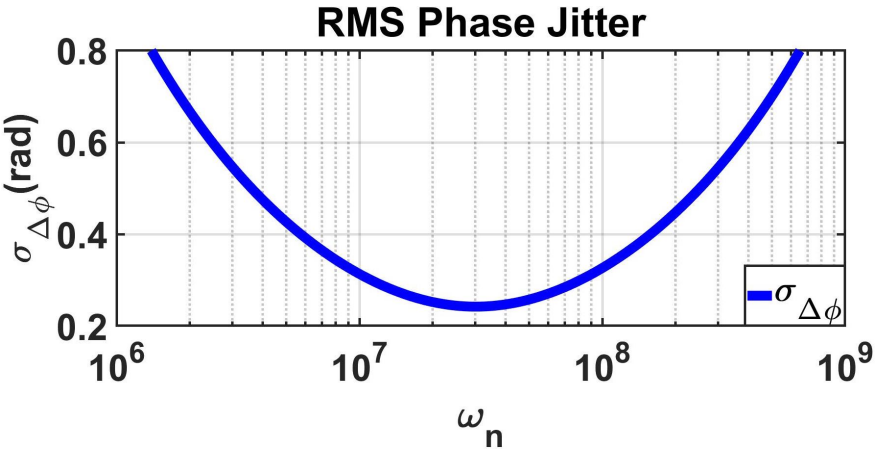

Figure 2.3: RMS phase jitter variation with respect to the natural frequency of the integer-N PLL.

As is clear from (2.14), $\sigma_{\Delta\phi_{PLL,\min}}$ for PLL-based synthesizers operating at higher frequencies and/or with wider tuning range will increase. $\sigma_{\Delta\phi_{PLL,\min}}$ can be further reduced to a lower-limit of $\sigma_{\Delta\phi_{PLL,\min}} = \sqrt{\eta M K_{clk} K_{VCO}}$ for sufficiently large ζ values at the cost of increasing the PLL acquisition time. Fig. 2.3 demonstrates variation of RMS phase jitter with respect to ω_n for $\zeta = 1$, $K_{VCO} = 2\pi \times 3$ GHz/V, $N = 280$, and $\eta = 10^{-14}$ V^2/Hz. It can be seen that under this condition, the RMS phase jitter is minimized for $\omega_n = 2\pi \times 4.8$ MHz to a value of 0.243 rad.

The timing jitter is also related to phase jitter, as follows

$$\sigma_{\Delta T} = \frac{\sigma_{\Delta\phi_{PLL}}}{2\pi f_0} \tag{2.15}$$

For instance, a 28-GHz PLL with a timing jitter of 65 fs, as reported in [35], has an RMS phase jitter of 0.011 rad.

In addition, the reference spurs induced by charge-pump leakage disturbs the phase noise profile of an integer-N PLL, and therefore, its impact should be quantified. Shown in Fig. 2.4a is the mechanism leading to generation of spurs (Fig. 2.4b). The charge-pump leakage current, I_{leak}, is modeled as a current source, which draws current from the PLL loop filter.

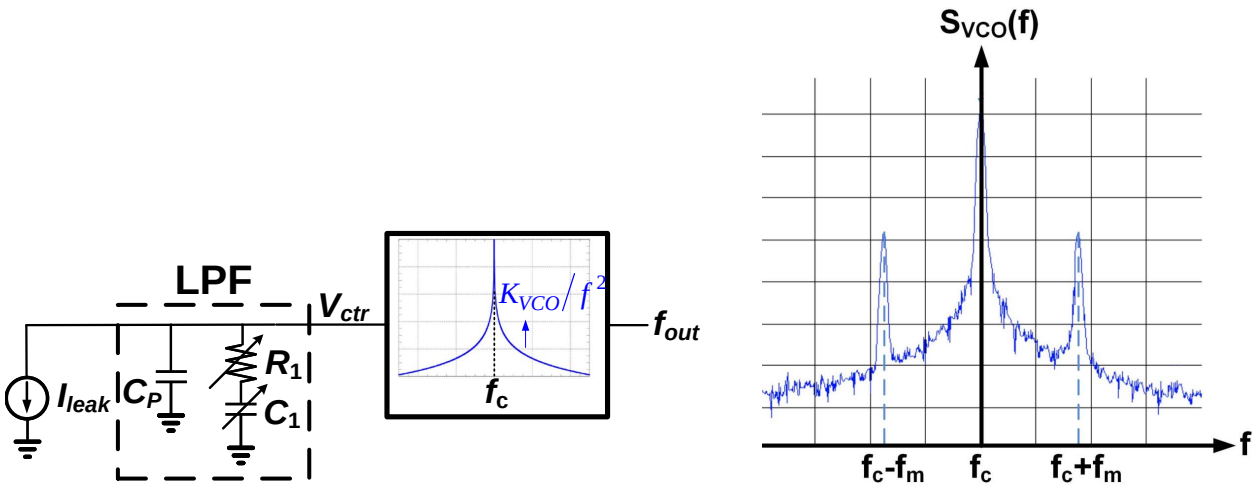

(a) (b)

Figure 2.4: (a) Current leakage of charge pumps resulting in spurs. (b) Output PSD of an integer-N PLL showing the spurs.

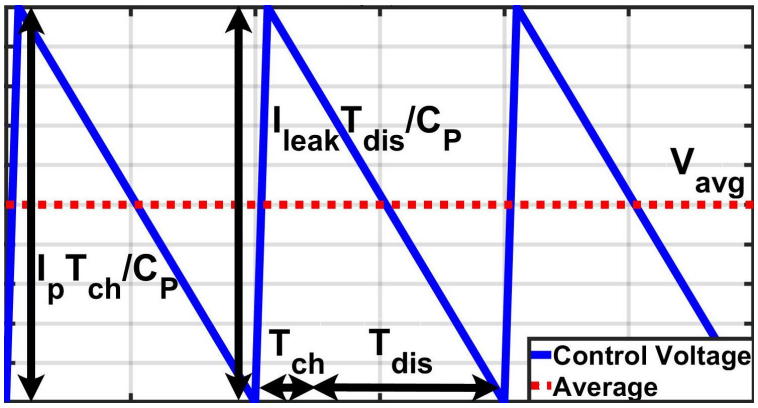

Figure 2.5: Control voltage waveform.

This current creates a disturbance, ΔV_{ctr}, on the control voltage, which is derived to be

$$\Delta V_{ctr} = -\frac{I_{leak}}{C_P}t \tag{2.16}$$

Under the locking condition, the PLL loop reacts to this disturbance by injecting a large current I_p compared to I_{leak} through the charge-pump to the loop filter such that the average value of the control voltage remains intact. Because of this large current surge, the corresponding charge time, T_{ch}, is much smaller than discharge time, T_{dis} (*cf.* Fig. 2.5), and the

control voltage looks approximately like a periodic sawtooth waveform [36]. This waveform can be decomposed into its frequency components using Fourier series expansion, as follows

$$V_{ctr} = V_{avg} - \frac{I_{leak}}{\pi C_P f_{in}} \sum_{n=1}^{\infty} \frac{\sin\left(2\pi n f_{in} t\right)}{n} \tag{2.17}$$

where f_{in} denotes the reference frequency. For every Fourier component of V_{ctr} (i.e., $A_m \sin\left(2\pi f_m t\right)$), the corresponding PLL output under the lock is:

$$V_{out} = A_c \cos\left(2\pi f_c t - \frac{K_{VCO} A_m}{2\pi f_m} \cos 2\pi f_m t\right) \tag{2.18}$$

where f_c is the PLL's oscillation frequency. Applying the narrow-band FM approximation, the output voltage becomes

$$\begin{aligned} V_{out} &= A_c \cos\left(2\pi f_c t\right) + \frac{K_{VCO} A_m}{4\pi f_m} A_c \sin\left(2\pi\left(f_c + f_m\right) t\right) \\ &+ \frac{K_{VCO} A_m}{4\pi f_m} A_c \sin\left(2\pi\left(f_c - f_m\right) t\right). \end{aligned} \tag{2.19}$$

Referring to Eqs. (2.17) and (2.19), the power of the n^{th} harmonic spur, P_n, with respect to the carrier power, P_C, is derived to be:

$$\frac{P_n}{P_C} = \frac{K_{VCO}^2 I_{leak}^2}{8\pi^4 n^4 f_{in}^4 C_P^2} \tag{2.20}$$

The higher-order spur harmonics are primarily filtered out by the PLL, leaving only the fundamental spur component to be the predominant source of impairment. In fact, a comparison with an analysis that accounts for all harmonics shows only 8% error. The phase jitter variance due to the spurs is thus approximately equal to:

$$\sigma_{\Delta\phi_s}^2 = \frac{1}{2}\left(\frac{K_{VCO} I_{leak}}{2\pi^2 f_{in}^2 C_P}\right)^2 \tag{2.21}$$

Using (2.13) and (2.21), the total RMS phase jitter (accounting for the spurs contribution) can be derived to be

$$\sigma_{\Delta\phi} = \sqrt{\sigma^2_{\Delta\phi_{PLL}} + \sigma^2_{\Delta\phi_s}} \tag{2.22}$$

Additionally, assuming the carrier to have unity power, the PSD associated with the carrier waveform and the PLL spurs, down-converted to the baseband, is derived to be:

$$S_{sp} = \sum_{n=1}^{\infty} P_n[\delta(f - nf_r) + \delta(f + nf_r)] \tag{2.23}$$

From Eq. (2.23), it is seen that the spurs' power varies in proportion to $1/n^4$. Therefore, the impact of spurs for $n \geq 2$ is negligible. Eq. (2.23) can thus be approximated by:

$$S_{sp} \approx P_1[\delta(f - f_r) + \delta(f + f_r)] \tag{2.24}$$

Moreover, one way of generating stable and low phase-noise LO at (sub-)THz frequency range is to employ a low-frequency PLL followed by a frequency multiplier. To account for the contribution of frequency multiplier to phase jitter, a periodic signal with phase perturbation, θ, is considered:

$$V_{in}(t) = \cos(2\pi f_c t + \theta) \tag{2.25}$$

Upon applying this signal to a frequency multiplier, the output signal becomes:

$$V_{out}(t) = \cos(2\pi\alpha f_c t + \alpha\theta + \beta) \tag{2.26}$$

where α and β are the multiplication factor and the phase-jitter stochastic process generated by the multiplier, respectively. It is inferred that the phase-noise stochastic process of the

output is increased by a factor of α even in the case of a noiseless multiplier (i.e., $\beta = 0$), resulting in an increase in RMS phase jitter by the same factor, α. Accounting for the phase-noise contribution of the multiplier and assuming that this noise is stochastically independent of the phase noise of the input signal (i.e., θ and β are independent processes), the total RMS phase jitter of the multiplier output signal, $\sigma_{\Delta\phi_M}$, is:

$$\sigma_{\Delta\phi_M} = \sqrt{\alpha^2\sigma_{\Delta\phi}^2 + \sigma_\beta^2} \tag{2.27}$$

where σ_β^2 is the phase jitter variance of the frequency multiplier. Therefore, if the LO circuit in a transceiver incorporates a lower-frequency PLL and a frequency multiplier, (2.27) will be used instead of (2.22) in forthcoming BER and EVM analyses.

The phased-locked-based synthesizer, such as the one in Fig. 2.1, is commonly used to generate the local oscillation in a wireless transceiver. A general block diagram of a radio transmitter is shown in Fig. 2.6a. The baseband stream appearing as pseudo-random bit sequence (PRBS) undergoes a number of signal processing blocks, most notably a digital modulator. The modulated data is mapped to analog domain by the mixed-signal block, and is subsequently upconverted to an RF frequency using LO mixing. The RF signal is then amplified by a power amplifier before being transmitted by the antenna. Conversely, in a radio receiver depicted in Fig. 2.6b, the received signal is amplified by a low-noise amplifier and downconverted to an intermediate frequency or directly to baseband by a phased-locked-based-LO mixing. Following the digitization by the mixed-signal part, the output bits are extracted by a digital demodulator.

The LO in any transceiver is thus always fed to an active or a passive mixer (e.g., a single-balanced active mixer shown in Fig. 2.7a) with a time-varying transconductance, $g_{sw}(t) = 2g_{m2}g_{m3}/(g_{m2} + g_{m3})$, shown in Fig. 2.7b. Although mixing operation appears to be a non-linear function relative to the LO amplitude, it is a linear function with respect to the LO

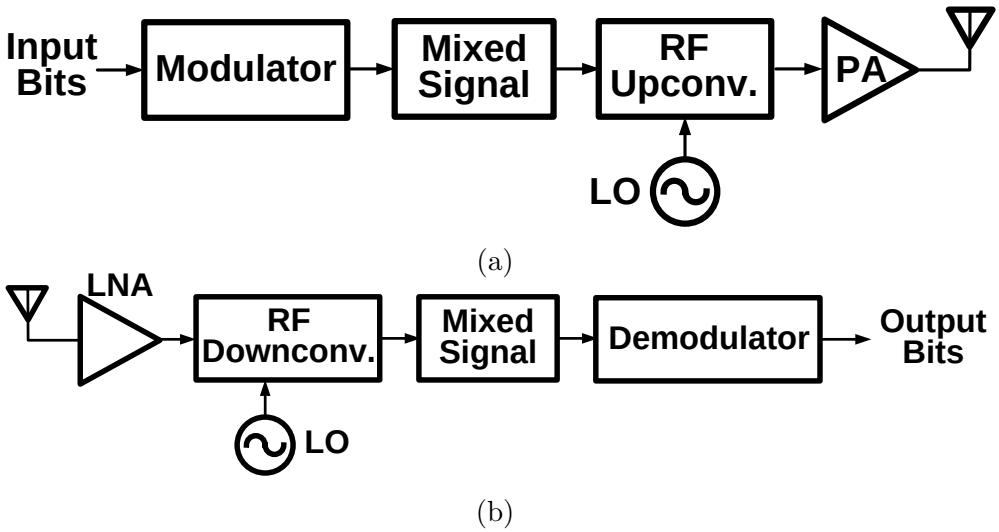

Figure 2.6: (a) Transmitter block diagram. (b) Receiver block diagram.

phase. Therefore, the LO jitter directly perturbs the RF signal's phase and zero-crossings. On the other hand, amplitude noise affects the RF chain through the mixer's switching action, as described below.

As has been discussed in [4] and [37], the mixer's output noise is a cyclostationary process. [38, 39] explained that a mixer cannot precisely track the existing random phase variation of its driving LO. It is thus conceivable to study the phase-randomized version of the mixer's output noise, which itself is a wide-sense stationary process whose statistical properties are the time-average of those of the output noise. More precisely, the time-average PSD is given by

$$S_{n,out}(f) = \sum_{k=-\infty}^{\infty} |g_{sw,k}|^2 S_{n,LO}(f - kf_{LO}) \tag{2.28}$$

where $g_{sw,k}$ is the Fourier series coefficients of $g_{sw}(t)$ and $S_{n,LO}$ is the equivalent noise PSD of the mixer referred to the LO port. Considering $S_{n,LO}(f)$ to be white with average power

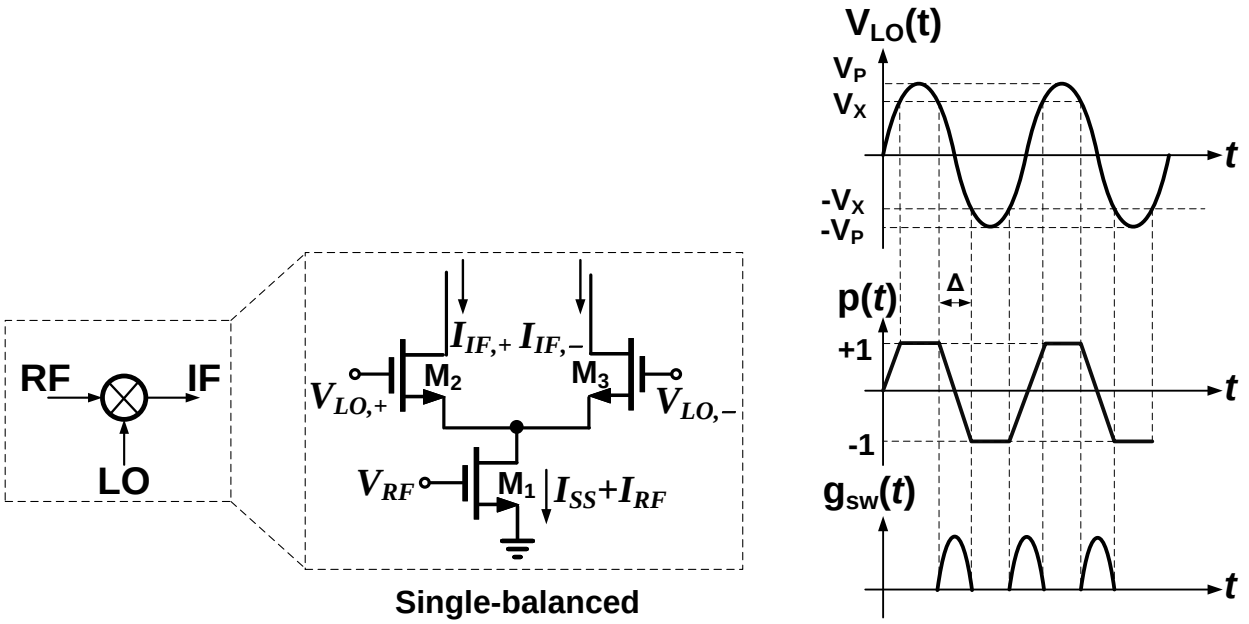

(a) (b)

Figure 2.7: (a) A single balanced current commutating mixer. (b) Time-varying transconductance, $g_{sw}(t)$, and switching function, $p\,(t)$.

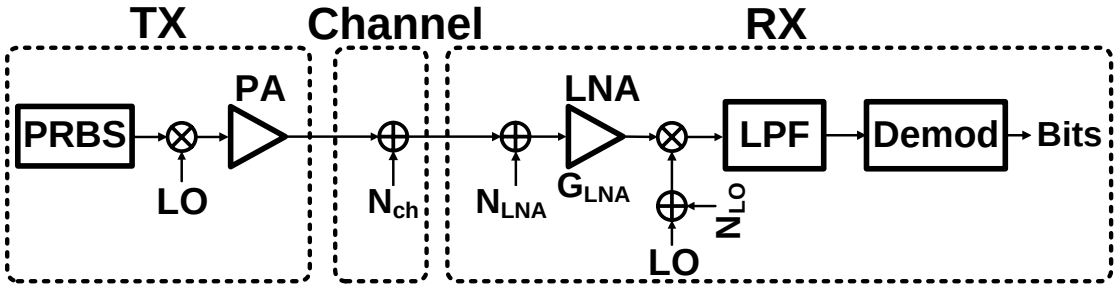

Figure 2.8: Block diagram of the communication link and its noise sources.

of N_{LO} (Fig. 2.8), the output noise power is:

$$N_{out} = N_{LO} \sum_{k=-\infty}^{\infty} |g_{sw,k}|^2, \tag{2.29}$$

which, using Parseval's theorem, is re-expressed as

$$N_{out} = N_{LO}\, \overline{g_{sw}^2(t)} \tag{2.30}$$

where $\overline{g_{sw}^2(t)}$ denotes the time average of $g_{sw}^2(t)$. To calculate the receiver equivalent noise

power, the mixer's output noise is referred back to its RF terminal. The input-referred instantaneous noise voltage, $V_{n,RF}(t)$, due to the mixer's output noise current, $I_{n,out}(t)$, is

$$V_{n,RF}(t) = \frac{I_{n,out}(t)}{g_{m,RF}\, p(t)} \tag{2.31}$$

where $g_{m,RF}$ is the transconductance of the tail transistor M_1 and $p\,(t)$ models the switching function of transistor pair M_2-M_3 in Fig. 2.7a. In this case, $\overline{p^2\,(t)}$ is calculated to be:

$$\overline{p^2\,(t)} = 1 - \frac{4}{3\pi} \sin^{-1}\left(\frac{V_X}{V_P}\right), \tag{2.32}$$

where V_X is the voltage at which complete switching of the differential pair takes place, and V_P is the LO voltage amplitude. Assuming hard switching, $\overline{p^2\,(t)} = 1$. The time-average PSD of the cyclostationary process, $I_{n,out}$, is derived to be:

$$S_{n,out}\,(f) = g_{m,RF}^2 \sum_{k=-\infty}^{\infty} |p_k|^2 S_{n,RF}\,(f)\,, \tag{2.33}$$

where $S_{n,RF}(f)$ is the PSD of the input-referred noise $V_{n,RF}(t)$. With $V_{n,RF}(t)$ being white and using Parseval's theorem, the noise power N_{RF} referred to the mixer's RF input is

$$N_{RF} = \frac{N_{out}}{g_{m,RF}^2\,\overline{p^2(t)}} = \frac{N_{LO}\,\overline{g_{sw}^2(t)}}{g_{m,RF}^2\,\overline{p^2(t)}} \tag{2.34}$$

This noise power is then referred back to the receiver input. Clearly, the overall noise power at the receiver input (N_{RX} in Fig. 2.8) should account for the predominant noise contribution of LNA, N_{LNA}. Therefore, using Friis equation, the receiver's input referred noise is

$$N_{RX} = N_{LNA} + \frac{N_{LO}\,\overline{g_{sw}^2(t)}}{g_{m,RF}^2\,\overline{p^2(t)}\,G_{LNA}} \tag{2.35}$$

where N_{LNA} is readily derived from LNA noise figure, NF_{LNA}, as follows

$$N_{LNA} = (NF_{LNA} - 1) \times 4kT\mathrm{Re}\{Z_{ant}\} \tag{2.36}$$

where $k = 1.38 \times 10^{-23}$ J/K is the Boltzmann constant, T is the absolute temperature in Kelvin, and Z_{ant} is the antenna impedance. N_{RX} is treated as part of link AWGN, which adds to the noise power of the channel (N_{ch} in Fig. 2.8) to give the total link AWGN (i.e., N_0).

2.2 Fractional-N Frequency Synthesizer

An integer-N frequency synthesizer is only capable of generating frequencies that are integer multiples of the reference frequency. This constraint creates several critical limitations in designing the PLL for a wireless TRX. For instance, the TX's output channel spacing must be equal to or a multiple integer of the reference frequency of an integer-N PLL. This, in turn, limits the loop bandwidth of the PLL and the extent to which the VCO phase noise is filtered by the loop. Fractional-N frequency synthesizers, on the other hand, overcome this limitation by enabling the TX to have smaller channel spacing relative to the reference frequency. Therefore, the PLL can have higher bandwidth, resulting in a reduction in settling time and phase noise[4, 40].

Fig. 2.9 depicts the block diagram of a fractional-N frequency synthesizer incorporating a $\Delta\Sigma$ modulator for modulus randomization. The modulator produces a binary random modulus control signal, denoted as $b(t)$, which assumes a binary state of either 0 or 1. Three predominant noise sources contribute to the overall noise performance of a fractional-N synthesizer, namely: (1) reference-clock phase noise, (2) VCO phase noise, and (3) quantization noise arising from the random modulus control signal. The reference and VCO phase noise

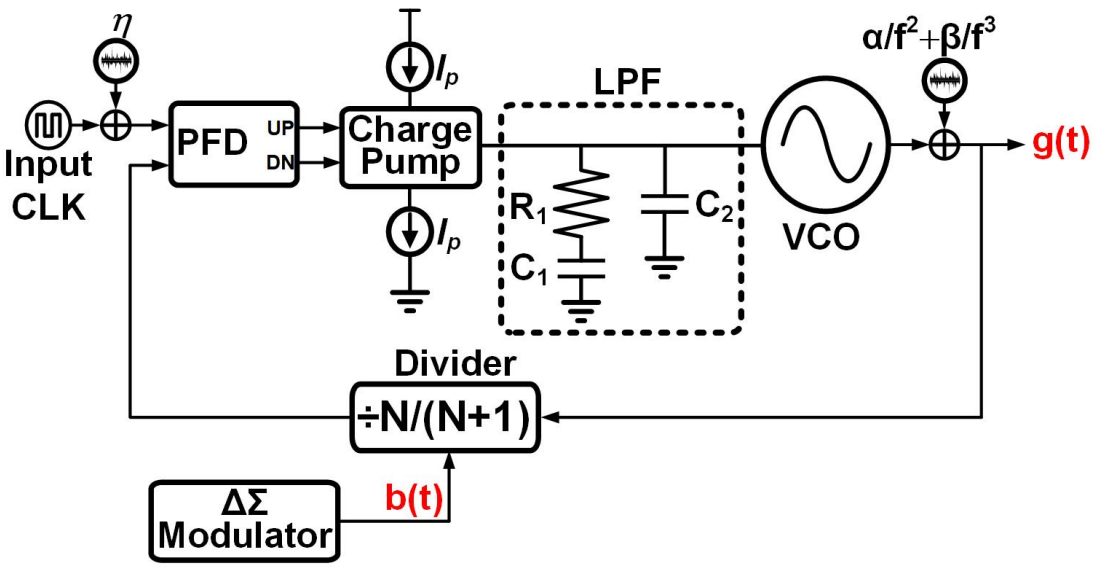

Figure 2.9: The block diagram of a fractional-N frequency synthesizer incorporating a $\Delta\Sigma$ modulator.

contributions to the PLL output phase noise were investigated in the previous section. As for the quantization noise contribution, defining B as $B = \mathbb{E}[b(t)]$ (where $\mathbb{E}$ denotes the expected value of a random variable and $0 \leq B \leq 1$), the instantaneous frequency of the divider's output is:

$$f_{FB}(t) = \frac{f_{out}}{N + B + q(t)} \tag{2.37}$$

where $q(t)$ represents the zero-mean quantization noise. If $q(t) \ll N + B$, Eq. (2.37) can be well-approximated by:

$$f_{FB}(t) = \frac{f_{out}}{N + B} - \frac{f_{out}}{(N + B)^2} q(t) \tag{2.38}$$

Given that the phase transfer functions from the divider output and the reference input to the PLL output are identical, the quantization noise is considered as the excess phase noise

of the reference. This excess phase-noise PSD is given by[4]:

$$S_{QZ}(f) = \left[\frac{f_r}{(N+B)f}\right]^2 S_q(f) \tag{2.39}$$

$S_q(f)$ is the PSD of $q(t)$, which is expressed by (2.40) [4]:

$$S_q(f) = \frac{B(1-B)}{f_r}\text{sinc}^2\left(\frac{f}{f_r}\right) \times |H(f)|^2 \tag{2.40}$$

where $H(f)$ is the transfer function of the noise shaping function and $\text{sinc}(x) = \sin(\pi x)/(\pi x)$ [41]. In the case where there is no noise shaping function, $H(f) = 1$, and for an L^{th}-order noise shaping function, $H(f)$ is:

$$H(f) = \left[2\sin\left(\frac{\pi f}{f_r}\right)\right]^L \tag{2.41}$$

Since the quantization noise and the reference clock phase noise are independent, the noise PSD due to the quantization noise referred back to the reference clock can be added to the reference clock original phase noise to calculate the total input phase noise, which is derived to be:

$$S_I(f) = \eta + \frac{B(1-B)f_r}{[(N+B)f]^2}\text{sinc}^2\left(\frac{f}{f_r}\right)\left|2\sin\left(\frac{\pi f}{f_r}\right)\right|^{2L} \tag{2.42}$$

Since the high-frequency components of Eq. (2.42) are filtered by the loop, only the low-frequency components are important. For $f \ll f_r$, (2.42) is simplified to:

$$S_I(f) = \eta + \frac{\lambda_L}{(N+B)^2}f^{2L-2} \tag{2.43}$$

where λ_L is defined as the quantization noise factor (QNF). λ_L represents a measure of the

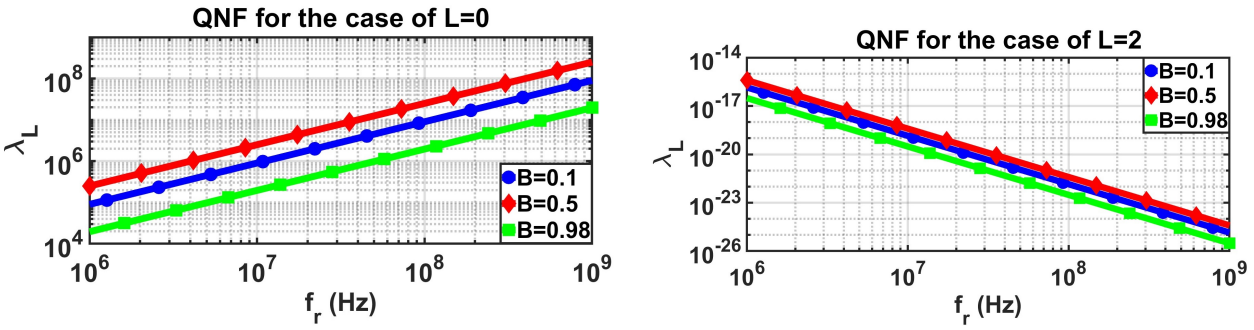

(a) (b)

Figure 2.10: QNF variation with respect to reference clock frequency when (a) no pulse shaping is being used, and (b) second-order pulse shaping is utilized.

quantization-noise impact on the PLL phase noise and is derived to be

$$\boxed{\lambda_L = \frac{(2\pi)^{2L} \times B(1-B)}{f_r^{2L-1}}} \tag{2.44}$$

It is readily observed that QNF is a positive quantity, and in the presence of noise shaping (i.e., $L \geq 1$), monotonically decreases with the reference frequency and assumes a peak at $B = 0.5$. On the other hand, in the absence of pulse shaping, QNF increases with the clock reference frequency. Figs. 2.10a-2.10b show the variation of QNF with respect to reference clock frequency for three distinct values of B.

To quantify the impact of quantization noise on the PLL's output phase-noise PSD, every η in (2.6) is replaced by $S_I(f)$ in (2.42). $S_\Phi(f)$ at low and high frequencies becomes:

$$S_\Phi(f)\Big|_{low\ f} = S_R + \lambda_L f^{2L-2} \tag{2.45}$$

$$S_\Phi(f)\Big|_{high\ f} = \frac{\alpha + 4\zeta^2 f_n^2 S_R}{f^2} \tag{2.46}$$

where $S_R = (N+B)^2\eta$ captures the contribution of the reference phase noise to the PLL

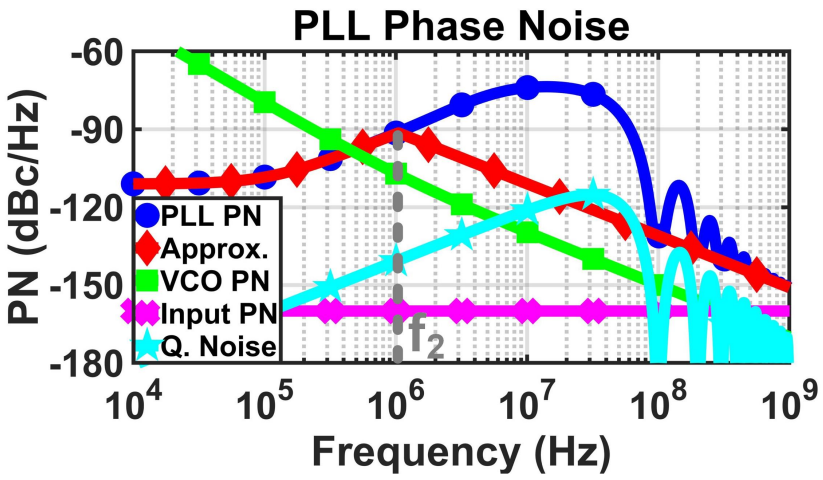

Figure 2.11: PLL phase noise profile and its approximation.

output. $S_\Phi(f)$ is thus approximated by:

$$\boxed{S_\Phi(f) = \begin{cases} S_R + \lambda_L f^{2L-2} & f \leq f_2 \\ (\alpha + 4\zeta^2 f_n^2 S_R)/f^2 & f > f_2 \end{cases}} \tag{2.47}$$

where f_2 is found by solving the following equation:

$$\lambda_L f_2^{2L} + S_R f_2^2 = \alpha + 4\zeta^2 f_n^2 S_R \tag{2.48}$$

Two special cases, L = 1 and L = 2, are of great interest. For L = 1, f_2 is:

$$f_2 = \sqrt{\frac{(2\zeta f_n)^2 + \alpha/S_R}{1 + \lambda_1/S_R}}, \tag{2.49}$$

and for L = 2, f_2 becomes:

$$f_2 = \sqrt{\frac{S_R}{2\lambda_2}\left[\sqrt{1 + \frac{4\lambda_2}{S_R}\left[(2\zeta f_n)^2 + \frac{\alpha}{S_R}\right]} - 1\right]} \tag{2.50}$$

Referring to Eq. (2.48), it is easily proved that $f_2 < f_1$, and if $\lambda_L \to 0$, then, $f_2 \to f_1$. Consequently, the phase noise profile of a fractional-N PLL behaves similarly to that of an

integer-N counterpart. Assuming $B = 0.3$ for the type-II PLL with design parameters used in the previous section, Fig. 2.11 shows plots of $S_\Phi(f)$ and its estimation as well as the reference and VCO phase noise profiles and the quantization noise. This plot verifies the accuracy of this approximation for the major part of the plot. It is noteworthy that if the modulus signal is randomized, the mechanism of spur generation in the fractional-N PLL is the same as the integer-N PLL. Therefore, same equations that characterized the integer-N PLL spurs can be used to characterize the fractional-N PLL in terms of its output spurs.

Chapter 3

PSK BER and EVM Degradations Due to PLL Jitter and Link AWGN

In what follows, BER and EVM degradations due to the PLL jitter and the link AWGN for widely used M-ary PSK schemes are analyzed.

3.1 BER of M-ary PSK Modulation Scheme

To underscore the effect of the PLL jitter on BER, the M-ary PSK signal is assumed to be upconverted by a noiseless LO. Neglecting the additive noise of the link momentarily, the received signal is downconverted by an LO whose RMS phase jitter is expressed by (2.22). Shown in Fig. 3.1a is the QPSK receiver constellation diagram, where the red crosses denote the ideal points and the blue dots indicate the constellation diagram subject to an RMS phase jitter of 0.1615 rad.

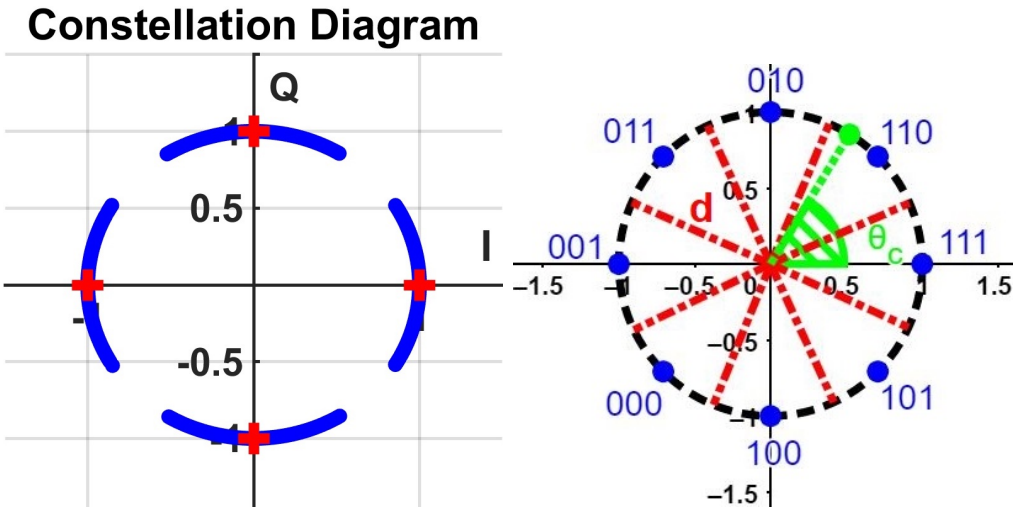

(a) (b)

Figure 3.1: (a) Receiver constellation diagram for QPSK. (b) Ideal 8PSK constellation diagram with symbols mapped in Gray code.

To begin with, the PDF of the normally distributed LO phase jitter is expressed as:

$$f_{\Theta}(\theta) = \frac{1}{\sigma_{\Delta\phi} \times \sqrt{2\pi}} e^{-\frac{\theta^2}{2\times\sigma_{\Delta\phi}^2}} \tag{3.1}$$

where θ is the phase-jitter stochastic process. To derive BER, a symbol error occurs whenever the received symbol falls outside its decision region. Fig. 3.1b shows an ideal 8PSK constellation diagram with Gray-coded symbols, where θ_c is the phase of a given symbol on the constellation diagram. For symbols that are transmitted at 0 rad, an error-free detection occurs if $-\frac{\pi}{M} < \theta_c < \frac{\pi}{M}$. Accounting for an RMS phase jitter of $\sigma_{\Delta\phi}$, the probability of error is given by

$$P_e|_{\theta_c=0} = P\left(\theta > \frac{\pi}{M}\right) + P\left(\theta < -\frac{\pi}{M}\right) = 2Q\left(\frac{\frac{\pi}{M}}{\sigma_{\Delta\phi}}\right) \tag{3.2}$$

where Q denotes the Q-function [27], which is the tail probability function of the standard normal distribution. Assuming each symbol is equally probable, the probability of transmit-

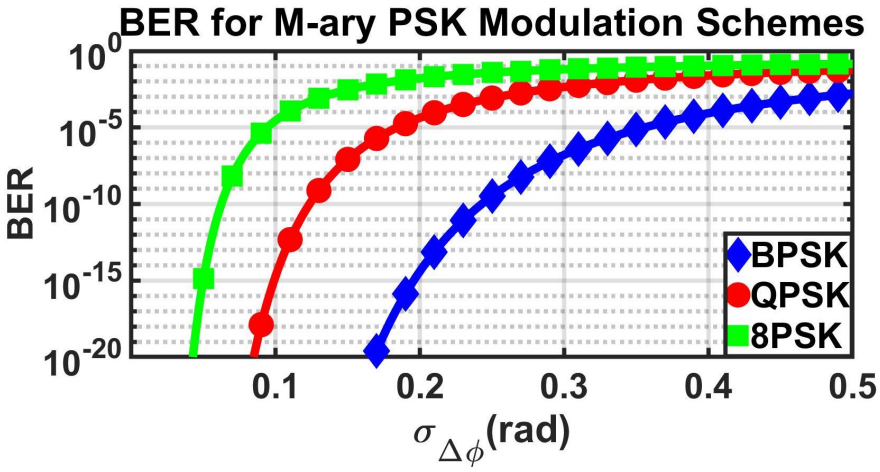

(a)

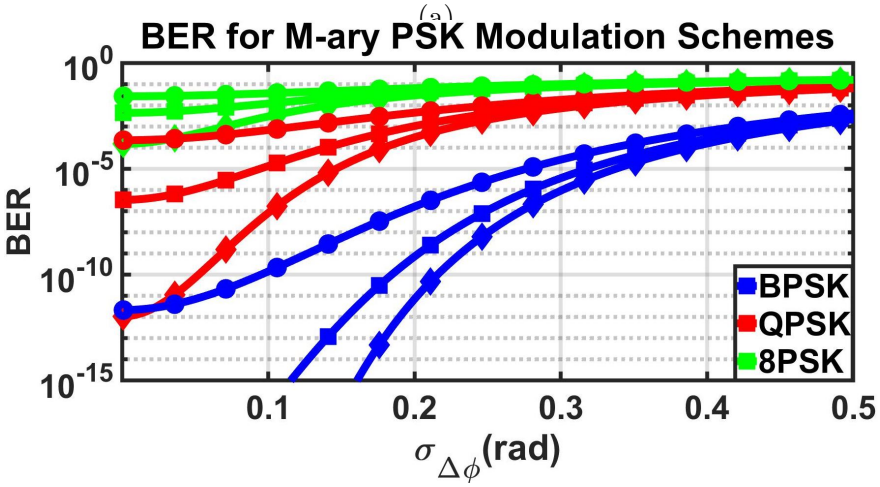

(b)

Figure 3.2: Plots of BER for M-ary PSK in the presence of (a) PLL jitter. (b) PLL jitter and link AWGN ($\rho_{min} = 10$ (≈ 10 dB) indicated by circle marker, $\rho_{min} = 20$ (≈ 13 dB) by square marker, and $\rho_{min} = 40$ (≈ 16 dB) by diamond marker).

ting each one of them is $\frac{1}{M}$. The symbol error rate (SER) is thus equal to

$$SER_{PSK} = 2Q\left(\frac{\frac{\pi}{M}}{\sigma_{\Delta\phi}}\right) \tag{3.3}$$

From Eq. (3.3), BER of the Gray-coded M-ary PSK symbols is given by

$$BER_{PSK} = \frac{2}{\log_2 M} Q\left(\frac{\frac{\pi}{M}}{\sigma_{\Delta\phi}}\right) \tag{3.4}$$

Plotted in Fig. 3.2a, Eq. (3.4) indicates that BER in an M-ary PSK system increases almost exponentially for small $\sigma_{\Delta\phi}$ and plateaus for its larger values. It is noteworthy that Eq. (3.4) was derived under the assumption that $\sigma_{\Delta\phi}$ is relatively small. For cases where the LO jitter becomes extremely large (i.e., $\sigma_{\Delta\phi} > \frac{\pi}{M}$), a considerable percentage of received symbols may rotate even farther than the next adjacent ones, thereby causing an error of more than one bit per symbol. The probability that a symbol is rotated more than $\frac{3\pi}{M}$ in the constellation diagram is, however, extremely small, making (3.4) valid for practical systems with BER's less than 10^{-2}.

To account for the effect of link AWGN, suppose the transmitted signal vector is represented as $s = \left(\sqrt{S_s}, 0\right)$, where S_s is the symbol power. Taking into account the effect of the link AWGN, the received symbol is $r = \left(\sqrt{S_s} + n_c, n_s\right)$ with n_c and n_s denoting in-phase and quadrature noise components, respectively. Since n_c and n_s are jointly Gaussian random variables with $\sigma_r^2 = \frac{N_0}{2} = \frac{N_{ch}+N_{RX}}{2}$, the PDF of vector $r = (r_1, r_2)$ is given by

$$f_r\left(r_1, r_2\right) = \frac{1}{2\pi\sigma_r^2} e^{-\frac{\left[\left(r_1-\sqrt{S_s}\right)^2+r_2^2\right]}{2\sigma_r^2}} \tag{3.5}$$

The random phase fluctuation, induced by link AWGN, around each symbol is defined as $\Theta_r = \tan^{-1}\left(r_2/r_1\right)$, whose PDF is:

$$f_{\Theta_r}\left(\theta_r\right) = \frac{1}{\pi} e^{-\rho_s \sin^2\theta_r} \int_0^\infty v e^{-\left(v-\sqrt{\rho_s}\cos\theta_r\right)^2} dv \tag{3.6}$$

where $\rho_s = S_s/(N_{ch} + N_{RX})$ is the symbol SNR and is readily expressed with respect to bit SNR $\rho_b = S_b/N_0$ as $\rho_s = \rho_b \times \log_2 M$. For large SNRs and $|\Theta_r| \leqslant \frac{\pi}{2}$, $f_{\Theta_r}\left(\theta_r\right)$ is simplified to

$$f_{\Theta_r}\left(\theta_r\right) \approx \sqrt{\frac{\rho_s}{\pi}} \cos\left(\theta_r\right) e^{-\rho_s \sin^2\theta_r} \tag{3.7}$$

Fig. 3.3 shows plots of PDFs from Eqs. (3.6) (in solid lines) and (3.7) (in asterisks) for three

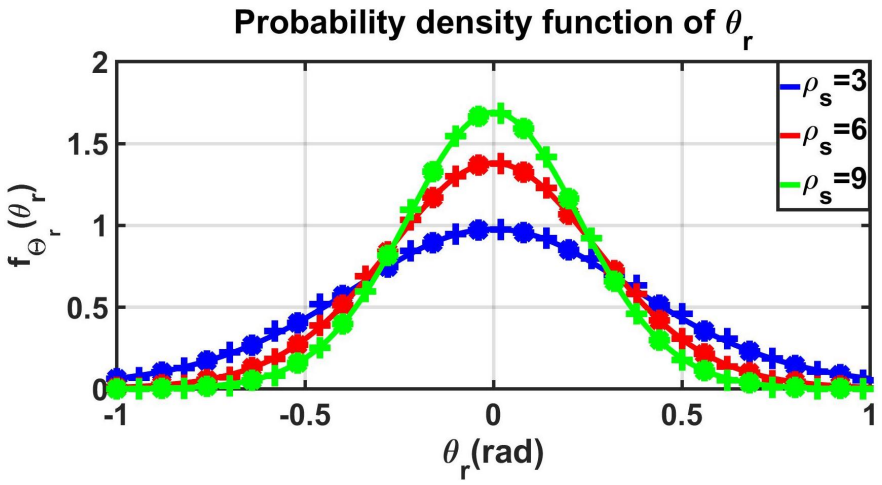

Figure 3.3: Probability density function of θ_r.

values of ρ_s with both plots closely following one another. Referring to Fig. 3.3, (3.7) can be approximated (to the first order) by a Gaussian distribution function with a zero mean and a variance of $\frac{1}{2\rho_s}$ (indicated by plus sign (+) marker in Fig. 3.3), i.e.,

$$f_{\Theta_r}(\theta_r) \approx \sqrt{\frac{\rho_s}{\pi}} e^{-\rho_s \theta_r^2} \tag{3.8}$$

Since LO phase jitter and link AWGN are independent, the PDF of sum of these random processes is calculated by convolving their PDFs (see [42]) in (3.1) and (3.8), i.e.,

$$\begin{aligned} f_{\Theta_t}(\theta_t) &= f_{\Theta}(\theta) * f_{\Theta_r}(\theta_r) \\ &= \frac{1}{\sigma_{\Delta\phi_t} \times \sqrt{2\pi}} e^{-\frac{\theta_t^2}{2\times\sigma_{\Delta\phi_t}^2}} \end{aligned} \tag{3.9}$$

where θ_t is the total phase-jitter stochastic process, and $\sigma_{\Delta\phi_t}$ is the total RMS phase jitter due to both LO jitter and the link AWGN, and is given by

$$\sigma_{\Delta\phi_t} = \sqrt{\sigma_{\Delta\phi}^2 + \frac{1}{2\rho_s}} \tag{3.10}$$

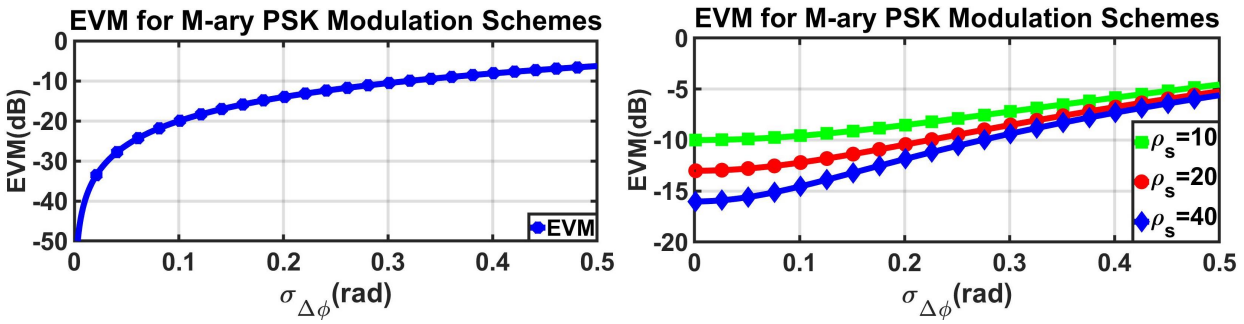

(a) (b)

Figure 3.4: Plots of EVM in dB for M-ary PSK in the presence of (a) PLL jitter. (b) PLL jitter and link AWGN.

To account for both LO jitter and AWGN in a wireless communication system, (3.10) instead of (2.22) can be used in all preceding BER equations. The BER for M-ary PSK in this general case is plotted in Fig. 3.2b for $\rho_s = 10$ (= 10 dB), $\rho_s = 20$ ($\approx$ 13 dB), and $\rho_s = 40$ ($\approx$ 16 dB). It is observed that BER in this case reaches a floor (e.g., 3.4×10^{-7} for QPSK and $\rho_s = 13$ dB) whose value is lowered with higher ρ_s values.

3.2 EVM for M-ary PSK Modulation Scheme

The RMS phase jitter, $\sigma_{\Delta\phi}$, of the PLL-based LO in a wireless transceiver introduces itself as a rotation to the M-ary PSK constellation. The average symbol power (ASP) in an M-ary PSK constellation is equal to d^2 where d is the distance from the origin to the ideal M-ary PSK constellation points. The mean square of the error vector (EV) caused by a random phase jitter of θ is readily derived, i.e.,

$$\overline{|EV_{\sigma_{\Delta\phi}}|^2} = 2d^2\left(1 - e^{-\frac{\sigma_{\Delta\phi}^2}{2}}\right) \tag{3.11}$$

Therefore, EVM for an M-ary PSK signal in the presence of LO jitter (and with no AWGN present) is derived:

$$EVM_{PSK} = \sqrt{\frac{\overline{|EV_{\sigma_{\Delta\phi}}|^2}}{ASP}} = \sqrt{2\left(1 - e^{-\frac{\sigma_{\Delta\phi}^2}{2}}\right)} \tag{3.12}$$

This result is consistent with the one obtained in [43]. Fig. 3.4a shows a plot of Eq. (3.12), where the EVM exhibits a saturating characteristic for large $\sigma_{\Delta\phi}$ values. This is because the maximum value of EV in a communication link with no AWGN is $2d$. Equivalently, for excessively large $\sigma_{\Delta\phi}$ values in Eq. (3.12), EVM reaches its worst value of 3 dB. Moreover, Eq. (3.12) can be further simplified for lower $\sigma_{\Delta\phi}$ values (i.e., $\sigma_{\Delta\phi} < 0.4$ rad), showing a linear growth, i.e., $EVM_{PSK} \approx \sigma_{\Delta\phi}$. An inspection of (3.12) reveals that increasing the signal power has no impact on EVM when the LO jitter is the sole source of impairment.

To capture the impact of the link AWGN on EVM, consider the symbol $(I, Q) = (\sqrt{S_x}, \sqrt{S_y})$ in which S_x and S_y are in-phase and quadrature components of the signal power, respectively. Assuming the transmitted signal vector to be $s = \left(\sqrt{S_x}, \sqrt{S_y}\right)$, the received symbol vector subject to link AWGN is $r = \left(\sqrt{S_x} + n_c, \sqrt{S_y} + n_s\right)$. Similar to previous section, n_c and n_s are also jointly Gaussian random variables with $\sigma_r^2 = \frac{\eta \times BW}{2} = \frac{N_0}{2}$ (BW is the system bandwidth). The PDF of vector r is given by

$$f_r\left(r_1, r_2\right) = \frac{1}{2\pi\sigma_r^2} e^{-\frac{\left[(r_1 - \sqrt{S_x})^2 + (r_2 - \sqrt{S_y})^2\right]}{2\sigma_r^2}} \tag{3.13}$$

Changing the coordinates from Cartesian to polar, $V = \sqrt{r_1^2 + r_2^2}$ represents the symbol distance from the origin and $\Phi = \tan^{-1}\left(r_2/r_1\right)$ indicates its angle from the positive x-axis. It is readily shown that in large SNR regimes (i.e., $\frac{S_x + S_y}{N_0} > 2$), the marginal PDFs can be

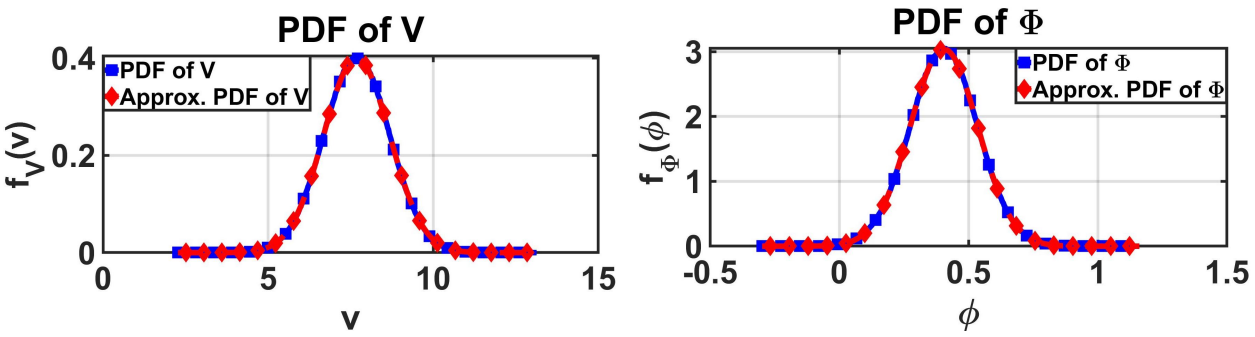

(a) (b)

Figure 3.5: (a) Probability density function of random variable V. (b) Probability density function of random variable Φ

well approximated using Gaussian PDF, as follows

$$f_V(v) \approx \frac{1}{\sigma_r\sqrt{2\pi}} e^{-\frac{\left(v-\sqrt{S_x+S_y+\frac{N_0}{2}}\right)^2}{2\sigma_r^2}} \tag{3.14}$$

$$f_\Phi(\phi) \approx \frac{1}{\sqrt{2\pi \times \frac{\sigma_r^2}{S_x+S_y}}} e^{-\frac{\left(\phi-\tan^{-1}(S_y/S_x)\right)^2}{2\sigma_r^2/(S_x+S_y)}} \tag{3.15}$$

Figs. 3.5a and 3.5b demonstrate PDFs of V and Φ, respectively, for normalized values $\frac{N_0}{2}=1$, $\sqrt{S_x}=7$, and $\sqrt{S_y}=3$, and compare the simulation results with approximations from Eqs. (3.14) and (3.15), where a good agreement between the probability density functions and their approximations is observed.

The LO jitter, θ, is added to the random phase of the RF signal, Φ. Given that θ and Φ are uncorrelated, the PDF of sum of them, $f_{\Theta_t}(\theta_t)$, is convolution of their PDFs. With both of these processes being normally distributed, we have:

$$f_{\Theta_t}(\theta_t) \approx \frac{1}{\sqrt{2\pi \times \left(\frac{\sigma_r^2}{S_x+S_y}+\sigma_{\Delta\phi}^2\right)}} e^{-\frac{\left(\theta_t-\tan^{-1}(S_y/S_x)\right)^2}{2\times\left(\frac{\sigma_r^2}{S_x+S_y}+\sigma_{\Delta\phi}^2\right)}} \tag{3.16}$$

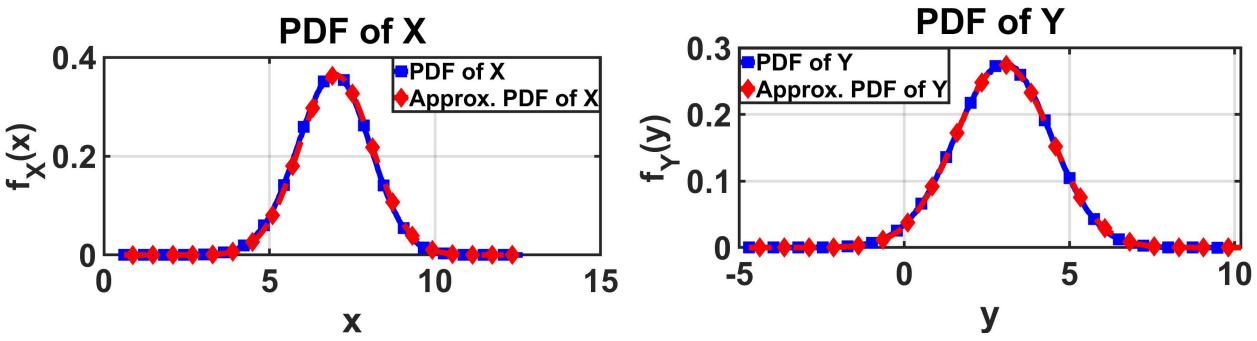

(a) (b)

Figure 3.6: (a) Probability density function of random variable X. (b) Probability density function of random variable Y

To derive EVM, the marginal PDFs in the Cartesian domain are calculated from Eqs. (3.14) and (3.16), i.e.,

$$f_X(x) \approx \frac{1}{\sqrt{2\pi \times \left(\sigma_r^2 + S_y \sigma_{\Delta\phi}^2\right)}} e^{-\frac{\left(x-\sqrt{S_x}\right)^2}{2\times\left(\sigma_r^2+S_y\sigma_{\Delta\phi}^2\right)}} \tag{3.17}$$

$$f_Y(y) \approx \frac{1}{\sqrt{2\pi \times \left(\sigma_r^2 + S_x \sigma_{\Delta\phi}^2\right)}} e^{-\frac{\left(y-\sqrt{S_y}\right)^2}{2\times\left(\sigma_r^2+S_x\sigma_{\Delta\phi}^2\right)}} \tag{3.18}$$

(3.17) and (3.18) provide good accuracy for $\sigma_{\Delta\phi}$ values seen in practice (e.g., $\sigma_{\Delta\phi} < 0.25$ rad). According to (3.17) and (3.18), X and Y are Gaussian random variables with $E\{X\} = \sqrt{S_x}$, $E\{Y\} = \sqrt{S_y}$ and $\sigma_X^2 = \sigma_r^2 + S_y\sigma_{\Delta\phi}^2$, $\sigma_Y^2 = \sigma_r^2 + S_x\sigma_{\Delta\phi}^2$, respectively. Figs. 3.6a and 3.6b demonstrate PDFs of X and Y, respectively, for $\sigma_{\Delta\phi} = 0.15$ rad and normalized values $\frac{N_0}{2} = 1$, $\sqrt{S_x} = 7$, $\sqrt{S_y} = 3$. A comparison with actual PDF plots verifies the accuracy of estimated PDFs in (3.17) and (3.18). Therefore, EV is derived to be:

$$\overline{|EV_{\sigma_{\Delta\phi}}|^2} = \overline{|EV_X|^2 + |EV_Y|^2} = N_0 + \sigma_{\Delta\phi}^2 (S_x + S_y) \tag{3.19}$$

In a PSK modulation scheme, $S_x + S_y = d^2$, therefore,

$$\overline{|EV_{\sigma_{\Delta\phi}}|^2} = N_0 + \sigma_{\Delta\phi}^2 d^2, \tag{3.20}$$

which results in

$$EVM_{PSK} = \sqrt{\sigma_{\Delta\phi}^2 + \frac{1}{\rho_s}} \tag{3.21}$$

It is noteworthy that (3.21) is consistent with the equation obtained in [43] for typical values of $\sigma_{\Delta\phi}$. It is inferred from (3.21) that EVM for an M-ary PSK system is equally affected by jitter variance and inverse of symbol SNR. Fig. 3.4b shows a plot of Eq. (3.21) for $\rho_s = 10$ (=10 dB), $\rho_s = 20$ ($\approx$ 13 dB), and $\rho_s = 40$ ($\approx$ 16 dB). It is observed again that EVM due to PLL jitter and link AWGN reaches a lower limit for a given symbol SNR (e.g., an EVM floor of -13 dB can be identified for $\rho_s = 13$ dB).

Chapter 4

QAM BER and EVM Degradations Due to PLL Jitter and Link AWGN

In what follows, BER and EVM degradations due to the PLL jitter and the link AWGN for widely used 4^MQAM schemes are analyzed.

4.1 BER for 4^MQAM Scheme

To better understand the impact of PLL jitter on the BER of a generic 4^MQAM scheme, the special case of a 16QAM constellation, indicated in Fig. 4.1a, with its symbols represented in Gray code is first studied. The x-axis (denoted by I) and y-axis (denoted by Q) of the diagram show the normalized in-phase and quadrature components, respectively.

As proved in Appendix A, only the first quadrant of the constellation plane needs to be analyzed with the remaining three yielding the same results. Additionally, a symmetry exists within the first quadrant referenced to the diagonal symbols (i.e., $i = q$ symbols). Therefore, the analysis is conducted only for the one-eighth of the constellation plane (i.e.,

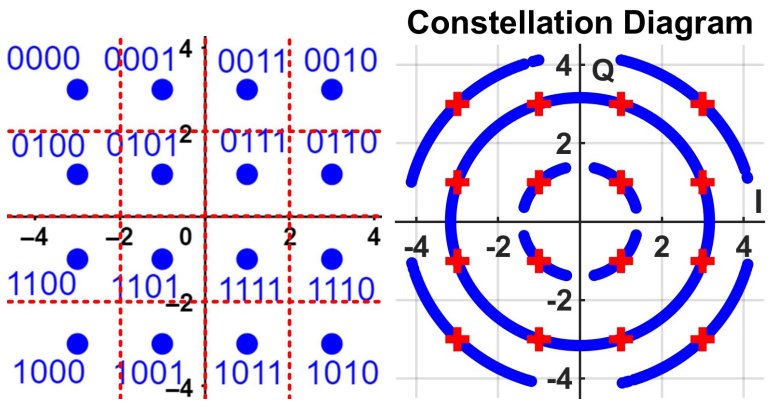

(a) (b)

Figure 4.1: (a) Ideal 16QAM constellation diagram with symbols mapped using Gray code. (b) Receiver constellation diagram for 16QAM.

$0 \leqslant \theta_c \leqslant \pi/4$).

Fig. 4.2a illustrates the rotational trajectory and the corresponding decision boundary of a diagonal symbol subject to PLL jitter. As proved in Appendix B, a jitter-induced error may cause erroneous detection of the neighboring left or bottom symbols of a diagonal symbol whose decision region falls within the angular interval given by

$$\sin^{-1}\frac{i-1}{\sqrt{2i^2}} < \theta_c < \cos^{-1}\frac{i-1}{\sqrt{2i^2}} \tag{4.1}$$

Those to the right of diagonal symbols (i.e., $i > q$) with an error might be detected ambiguously with their top or bottom symbols. According to Fig. 4.2b, the angular interval of the decision region for those symbols is

$$\sin^{-1}\frac{q-1}{\sqrt{i^2+q^2}} < \theta_c < \sin^{-1}\frac{q+1}{\sqrt{i^2+q^2}} \tag{4.2}$$

Finally, due to diagonal symmetry, for the symbols to the left of diagonal ones (i.e., $i < q$), the decision region is characterized by the angular interval given by

$$\cos^{-1}\frac{i+1}{\sqrt{i^2+q^2}} < \theta_c < \cos^{-1}\frac{i-1}{\sqrt{i^2+q^2}}, \tag{4.3}$$

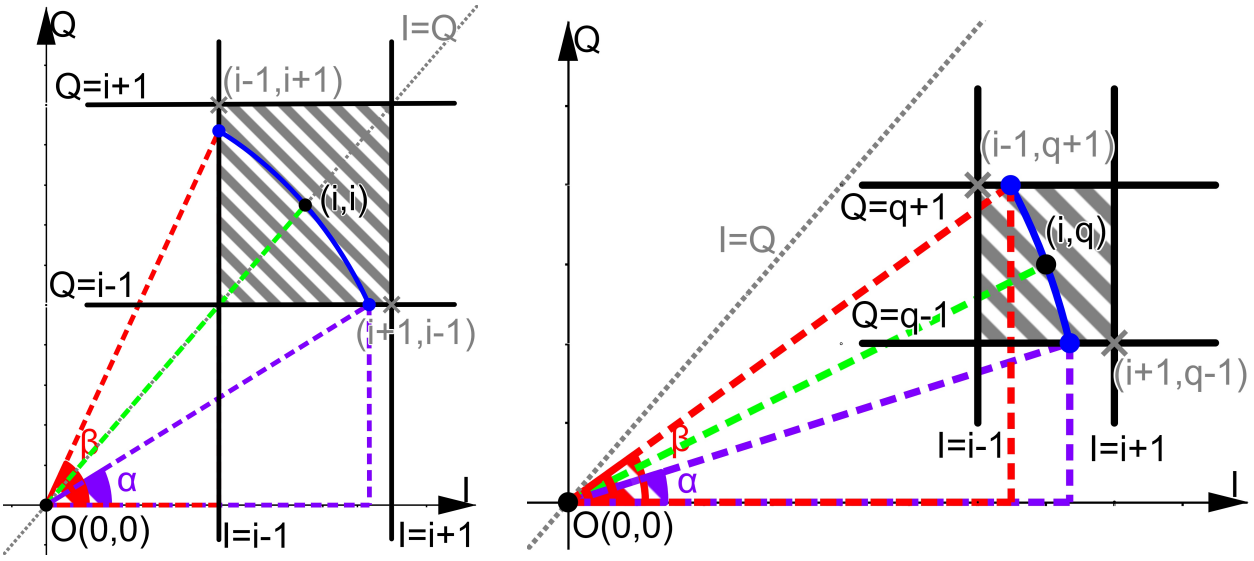

Figure 4.2: (a) Decision region for $i = q$ symbols. (b) Decision region for $i > q$ symbols.

which has the same angle of rotation as the following interval (see Appendix B)

$$\sin^{-1}\frac{i-1}{\sqrt{i^2+q^2}} < \theta_c < \sin^{-1}\frac{i+1}{\sqrt{i^2+q^2}}. \tag{4.4}$$

For instance, the decision regions for symbols $(I, Q) = (+3, +1)$ and $(I, Q) = (+1, +3)$ are $0 < \theta_c < \sin^{-1}(2/\sqrt{10})$ and $\cos^{-1}(2/\sqrt{10}) < \theta_c < \pi/2$, respectively. These two intervals cover the same angle of rotation, thereby producing the same probability of error.

(4.2) and (4.4) are combined into one inequality to represent the decision region for all symbols except the diagonal ones in a 4^MQAM constellation, as follows

$$\sin^{-1}\frac{\min(i,q)-1}{\sqrt{i^2+q^2}} < \theta_c < \sin^{-1}\frac{\min(i,q)+1}{\sqrt{i^2+q^2}} \tag{4.5}$$

In the case of 16QAM, for $(I, Q) = (+1, +1)$, the receiver will identify this symbol correctly if it lies within $0 < \theta_c < \pi/2$ based on (4.1). In the presence of an RMS phase jitter of $\sigma_{\Delta\phi}$,

the probability that a received symbol phase falls outside this interval is

$$P_e|_{(I,Q)=(+1,+1)} = 2Q\left(\frac{\frac{\pi}{4}}{\sigma_{\Delta\phi}}\right) \tag{4.6}$$

Similarly, for diagonal symbol $(I,Q) = (+3,+3)$, the probability of error is calculated to be

$$P_e|_{(I,Q)=(+3,+3)} = 2Q\left(\frac{\frac{\pi}{4} - \sin^{-1}\frac{2}{\sqrt{18}}}{\sigma_{\Delta\phi}}\right) \tag{4.7}$$

For the transmitted symbol $(I,Q) = (+3,+1)$, the error-free detection occurs if the received symbol lies within $0 < \theta_c < \sin^{-1}(2/\sqrt{10})$. The probability of error due to PLL jitter becomes

$$P_e|_{(I,Q)=(+3,+1)} = Q\left(\frac{\sin^{-1}\frac{2}{\sqrt{10}} - \sin^{-1}\frac{1}{\sqrt{10}}}{\sigma_{\Delta\phi}}\right) + Q\left(\frac{\sin^{-1}\frac{1}{\sqrt{10}}}{\sigma_{\Delta\phi}}\right)$$

which is the same as the probabilities of error for symbol $(I,Q) = (+1,+3)$.

Since the probability of transmitting each of the 16QAM symbols is $\frac{1}{16}$, the SER is derived to be:

$$\begin{aligned} SER_{16QAM} = \frac{1}{2} \times \Bigg[& Q\left(\frac{\frac{\pi}{4}}{\sigma_{\Delta\phi}}\right) + Q\left(\frac{\frac{\pi}{4} - \sin^{-1}\frac{2}{\sqrt{18}}}{\sigma_{\Delta\phi}}\right) \\ & + Q\left(\frac{\sin^{-1}\frac{2}{\sqrt{10}} - \sin^{-1}\frac{1}{\sqrt{10}}}{\sigma_{\Delta\phi}}\right) + Q\left(\frac{\sin^{-1}\frac{1}{\sqrt{10}}}{\sigma_{\Delta\phi}}\right)\Bigg] \end{aligned} \tag{4.8}$$

Assuming Gray-coded symbols, each symbol differs from the next one in exactly one bit. Therefore, the BER becomes

$$BER_{16QAM} = \frac{1}{\log_2 16} SER_{16QAM} = \frac{1}{4} SER_{16QAM} \tag{4.9}$$

Eq. (4.9) assumes that the error is relatively small. If the LO jitter becomes excessively large, some received symbols may fall farther than the next adjacent ones, thereby causing an error of more than one bit per symbol. In this case, the analysis underestimates the BER.

The simulated constellation diagram of a 16QAM system at the receiver side for an RMS phase jitter of $\sigma_{\Delta\phi} = 0.1615$ rad, neglecting the link AWGN, is shown in Fig. 4.1b, where the red crosses and blue dots indicate the ideal and actual points in the constellation diagram, respectively. It is observed that the LO jitter's detrimental effect becomes more severe for symbols farther away from the origin.

The foregoing analyses are generalized to 4^MQAM scheme. For a 4^MQAM signal subject to an RMS phase jitter of $\sigma_{\Delta\phi}$, since the probability of transmitting each symbol is $\frac{1}{4^M}$, the SER, and thus the BER, are readily calculated. The BER of Gray-coded 4^MQAM symbols with respect to SER is:

$$BER_{4^M QAM} = \frac{1}{\log_2 4^M} SER_{4^M QAM} = \frac{1}{2M} SER_{4^M QAM} \tag{4.10}$$

Using (4.1), the probability of error of each diagonal symbol is derived to be

$$P_e|_{(I,Q)=(O_n,O_n)} = 2Q\left(\frac{\frac{\pi}{4} - \sin^{-1}\frac{O_n - 1}{\sqrt{2O_n^2}}}{\sigma_{\Delta\phi}}\right), \tag{4.11}$$

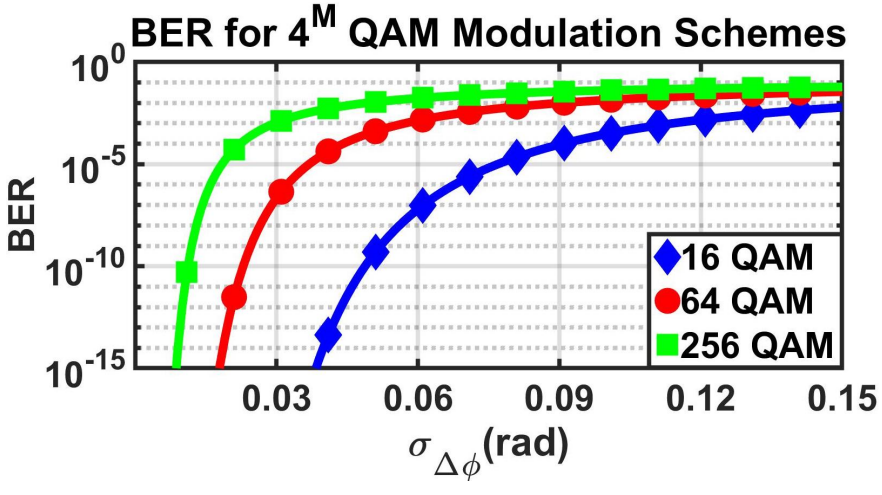

(a)

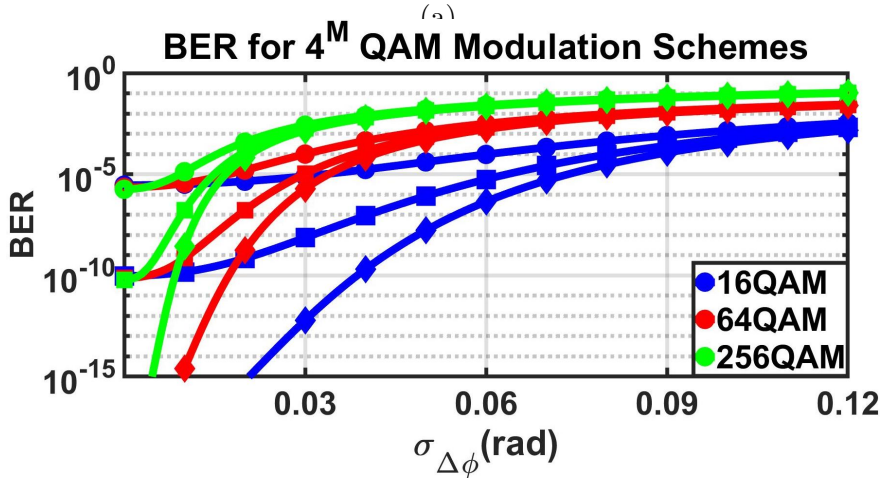

(b)

Figure 4.3: Plots of BER for 4^MQAM in the presence of (a) PLL jitter. (b) PLL jitter and link AWGN ($\rho_{min} = 10$ (≈ 10 dB) indicated by circle marker, $\rho_{min} = 20$ (≈ 13 dB) by square marker, and $\rho_{min} = 40$ (≈ 16 dB) by diamond marker).

and the probability of error of non-diagonal symbols is derived with the aid of (4.5), i.e.,

$$P_e|_{(I,Q)=(O_n,O_m)} = Q\left(\frac{\sin^{-1}\frac{\min(O_n,O_m)+1}{\sqrt{O_n^2+O_m^2}} - \sin^{-1}\frac{\min(O_n,O_m)}{\sqrt{O_n^2+O_m^2}}}{\sigma_{\Delta\phi}}\right) + Q\left(\frac{\sin^{-1}\frac{\min(O_n,O_m)}{\sqrt{O_n^2+O_m^2}} - \sin^{-1}\frac{\min(O_n,O_m)-1}{\sqrt{O_n^2+O_m^2}}}{\sigma_{\Delta\phi}}\right) \tag{4.12}$$

where $O_l = 2l - 1$ for $l \in \mathbb{N}$. Using (4.11) and (4.12), the BER for Gray-coded 4^MQAM

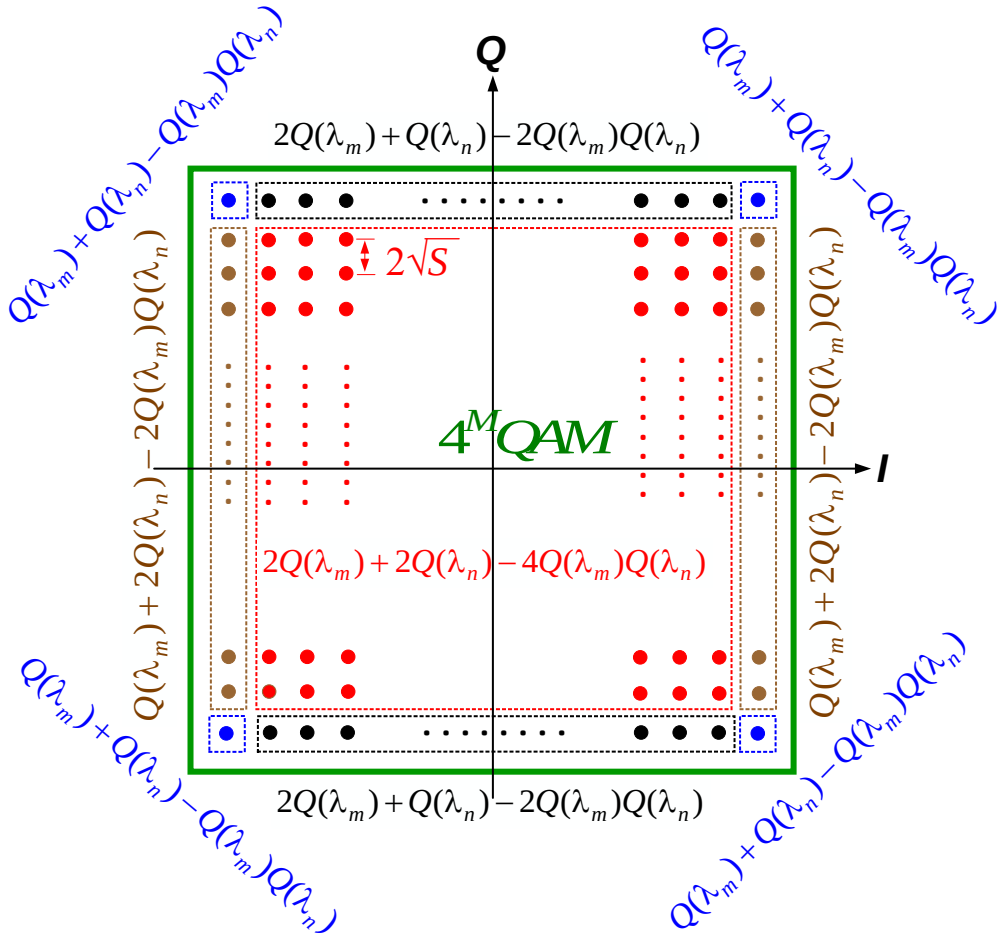

Figure 4.4: Probability of error calculation of QAM scheme.

symbols is expressed by (4.13) and shown in Fig. 4.3a.

$$BER_{4^M QAM} = \frac{1}{M \times 4^{M-1}} \times \left[\sum_{n=1}^{2^{M-1}} Q\left(\frac{\frac{\pi}{4} - \sin^{-1} \frac{O_n - 1}{\sqrt{2O_n^2}}}{\sigma_{\Delta\phi}} \right) + \sum_{n=2}^{2^{M-1}} \sum_{l=1}^{n-1} Q\left(\frac{\sin^{-1} \frac{\min(O_n, O_l)+1}{\sqrt{O_n^2+O_l^2}} - \sin^{-1} \frac{\min(O_n, O_l)}{\sqrt{O_n^2+O_m^2}}}{\sigma_{\Delta\phi}} \right) + Q\left(\frac{\sin^{-1} \frac{\min(O_n, O_l)}{\sqrt{O_n^2+O_m^2}} - \sin^{-1} \frac{\min(O_n, O_l)-1}{\sqrt{O_n^2+O_l^2}}}{\sigma_{\Delta\phi}} \right) \right] \tag{4.13}$$

It should be noted that (4.13) underestimates the actual BER in the presence of large PLL jitter. This is because the assumption that none of the symbols subject to error may fall farther than the next adjacent symbols becomes invalid for large values of PLL jitter. Therefore, an erroneous symbol may contain more than one false bit, and the actual BER

may thus be higher than the value predicted by Eq. (4.13).

Now, suppose a 4^MQAM constellation diagram in Fig. 4.4 with symbol spacing of $2\sqrt{S}$, where $\rho_{min} = \frac{S}{N_0}$ denotes the minimum SNR. The probability of error for an arbitrary symbol $(I, Q) = (n\sqrt{S}, m\sqrt{S})$, for $-2^M + 1 \leq n, m \leq 2^M - 1$, is derived using (3.17) or (3.18) depending on the symbol's location on the constellation diagram. An inner symbol (color-coded in red in Fig. 4.4) is correctly detected at the receiver side if $(n-1)\sqrt{S} < X < (n+1)\sqrt{S}$ and $(m-1)\sqrt{S} < Y < (m+1)\sqrt{S}$. The probability P_c of such detection is

$$P_c = (1 - 2Q(\lambda_n))(1 - 2Q(\lambda_m)) \tag{4.14}$$

where λ_l is a function of minimum SNR, ρ_{min}, and PLL-based LO jitter, i.e.,

$$\lambda_l = \frac{1}{\sqrt{\frac{1}{2\rho_{min}} + l^2\sigma_{\Delta\phi}^2}} \qquad \text{for} \quad l \in \mathbb{N} \tag{4.15}$$

The probability of error, $1 - P_c$, is readily calculated, as follows

$$P_e|_{(I,Q)=(n\sqrt{S}, m\sqrt{S})} = 2Q(\lambda_m) + 2Q(\lambda_n) - 4Q(\lambda_m)Q(\lambda_n) \tag{4.16}$$

Similarly, other symbols located on different parts of the constellation diagram are proved to have their own specific probabilities of error, as indicated in Fig. 4.4. Therefore, the probability of error, P_e, for each symbol is calculated.

Moreover, considering that the probability of transmitting each symbol is $\frac{1}{4^M}$ and each symbol differs from its neighboring symbols in exactly one bit, BER in the presence of both link AWGN and LO phase jitter is derived using the symbols' probabilities of error indicated in Fig. 4.4. Eq. (4.17) reveals this closed-form BER expression. Note that this equation (1) is accurate for high SNR transceivers (e.g., $BER < 10^{-2}$), and (2) becomes less accurate as

M increases because the marginal PDFs obtained in (3.17) and (3.18) can no longer be well approximated by Gaussian distribution.

Fig. 4.3b shows plots of the BER as estimated by Eq. (4.17) for $\rho_{min} = 10$ (=10 dB), $\rho_{min} = 20$ ($\approx$ 13 dB), and $\rho_{min} = 40$ ($\approx$ 16 dB), and for three modulation schemes, namely, 16QAM, 64QAM, and 256QAM. It is observed that (1) in extremely small phase-jitter regime, the order of modulation does not affect the BER as long as ρ_{min} is constant, and (2) the BER is negligibly influenced by SNR in high phase-jitter regime, and will increase with the modulation order.

$$\boxed{BER_{4^M QAM} = \frac{1}{M \times 4^{M-1}} \times \left[\left(2^M - 1 - 2Q\left(\lambda_{2^M-1}\right)\right) \times \sum_{n=1}^{2^{M-1}-1} Q\left(\lambda_{O_n}\right) - 2 \sum_{n=1}^{2^{M-1}-1} \sum_{l=1}^{2^{M-1}-1} Q\left(\lambda_{O_l}\right) Q\left(\lambda_{O_n}\right) + \left(2^M - 1 - \frac{1}{2} Q\left(\lambda_{2^M-1}\right)\right) \times Q\left(\lambda_{2^M-1}\right) \right]} \tag{4.17}$$

The inner symbols constitute $\left[1 - \left(2^M - 1\right)/2^{2M-2}\right] \times 100\%$, and hence majority, of all 4^MQAM symbols for larger values of M (e.g. $M \geq 4$). Accounting for this notion, we assume that all constellation points (i.e., inner, edge, and corner symbols) have approximately the same probability of error given by (4.16). This assumption allows for (4.17) to be approximated by a simplified form, as follows:

$$BER_{4^M QAM} \approx \frac{1}{M \times 4^{M-1}} \times \left[2^M \times \sum_{n=1}^{2^{M-1}} Q\left(\lambda_{O_n}\right) - 2 \sum_{n=1}^{2^{M-1}} \sum_{l=1}^{2^{M-1}} Q\left(\lambda_{O_l}\right) Q\left(\lambda_{O_n}\right) \right] \tag{4.18}$$

It is worth noting that (4.18) overestimates the BER because the edge and corner symbols are assigned values larger than their actual probabilities of error. As M increases, this overestimated BER approaches its actual value.

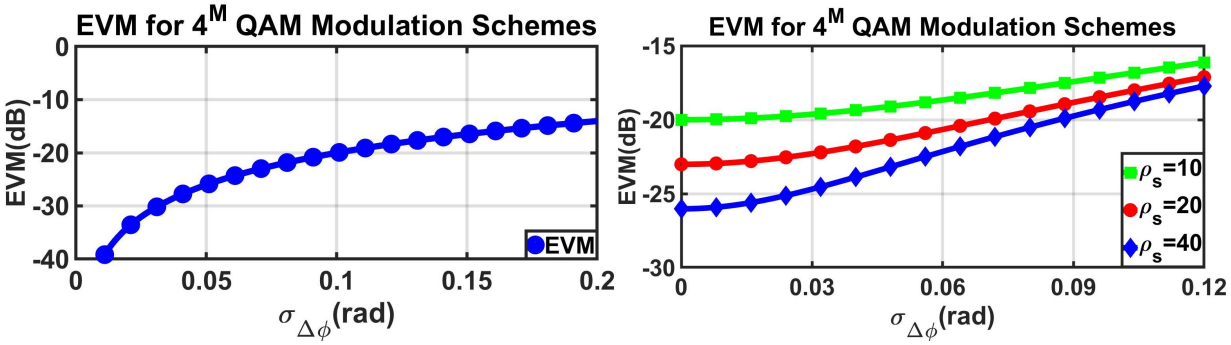

(a) (b)

Figure 4.5: Plots of EVM for 4^MQAM in the presence of (a) PLL jitter, and (b) PLL jitter and link AWGN.

4.2 EVM for 4^MQAM Scheme

Similar to the previous section and [43], EVM for 4^MQAM can be derived and proved to be identical to that of the PSK modulation scheme:

$$EVM_{4^MQAM} = \sqrt{2\left(1 - e^{-\frac{\sigma_{\Delta\phi}^2}{2}}\right)} \tag{4.19}$$

Fig. 4.5a demonstrates the EVM plot of Eq. (4.19) with respect to $\sigma_{\Delta\phi}$ and in the absence of link AWGN, exhibiting a saturating characteristic for large values of PLL jitter.

A comparison of (3.12) with (4.19) reveals that (1) the LO phase jitter exerts the same effect on the EVM for different modulation schemes and (2) the EVM due to LO phase jitter remains invariant with respect to the signal power. In summary, regardless of the symbol arrangement in a constellation diagram, the LO phase jitter exerts the same effect on the EVM if other noise sources are neglected.

To derive the EVM for the 4^MQAM scheme when both LO phase jitter and link AWGN are

present, (3.19) is utilized to first calculate the EV. This leads to

$$EVM_{4^MQAM} = \sqrt{\sigma^2_{\Delta\phi} + \frac{1}{\rho_{avg}}} \tag{4.20}$$

Notice that, in 4^MQAM schemes, the minimum SNR, ρ_{min}, and the average SNR, ρ_{avg}, are related, as follows

$$\rho_{avg} = \rho_{min} \times \frac{\sum_{m=1}^{2^{M-1}} \sum_{n=1}^{2^{M-1}} O_n^2 + O_m^2}{4^{M-1}} \tag{4.21}$$

Fig. 4.5b depicts plots of Eq. (4.20) for $\rho_{min} = 10$ (=10 dB), $\rho_{min} = 20$ ($\approx$ 13 dB), and $\rho_{min} = 40$ ($\approx$ 16 dB), demonstrating a similar trend as in M-ary PSK.

Chapter 5

The Impact of PLL Noise and Spurs on OOBE

The subsequent analysis in this chapter focuses on evaluating the impact of phase noise and spurs introduced by integer-N and fractional-N PLLs on OOBE. Referring to Fig. 5.1, the PLL produces quadrature LO signals, $g_I(t)$ and $g_Q(t)$, with identical PSD, $S_G(f)$. Similarly, the two input baseband signals, $x_I(t)$ and $x_Q(t)$, exhibit an identical PSD, $S_X(f)$.

Due to the switching operation of RF mixers, the baseband signal, $x(t)$, is multiplied by a periodic square wave, containing the odd harmonics of the LO signal, $g(t)$ [44]. With higher harmonics falling out of band, only the LO's first harmonic is taken into consideration. Therefore, the TX mixer's output signal is roughly assumed to be $y(t) = A_{V,MX} \times x(t) \times g(t)$, where $A_{V,MX}$ is the mixer conversion gain. $A_{V,MX}$ has no impact on the relative out-of-band power levels, as it uniformly increases both the in-band and out-of-band PSDs. Therefore, without loss of generality, $A_{V,MX}$ is assumed to be equal to one, hence, $y(t) = x(t) \times g(t)$. Assuming $g(t) = A_C \cos(2\pi f_c t + e(t))$, where $e(t)$ denotes the combination of phase noise and spur disturbance whose PSDs were calculated in the previous sections, the output signal

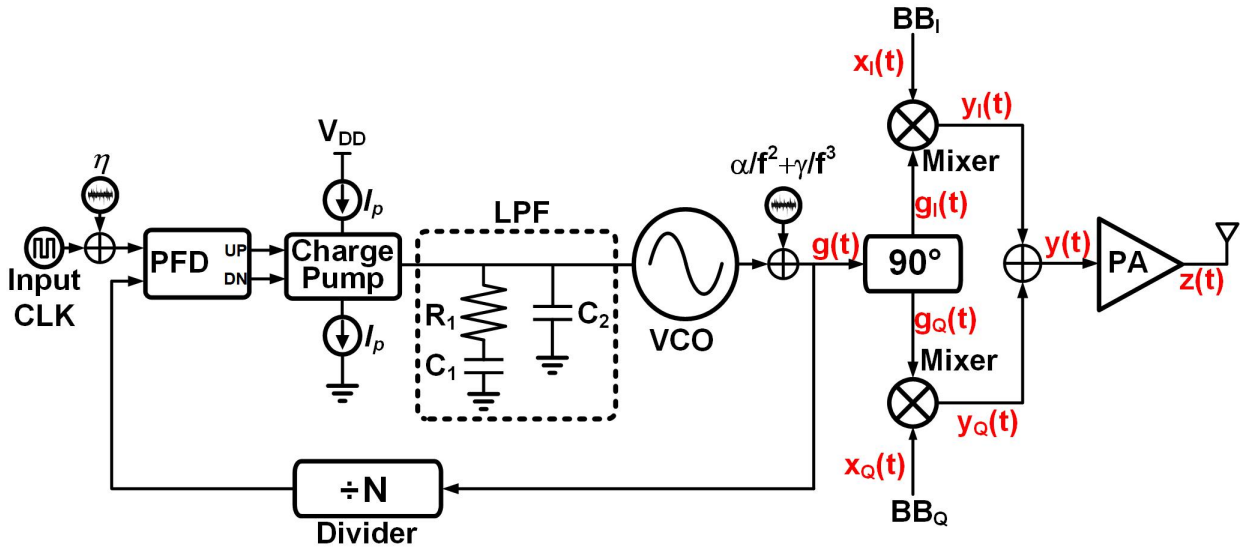

Figure 5.1: A basic direct-conversion TX block diagram.

is calculated to be:

$$y(t) = x(t) \times A_C \cos\left(2\pi f_c t + e(t)\right) \tag{5.1}$$

The output waveform in the time domain can be expressed as:

$$y(t) = A_C x(t) \times \left[\cos\left(2\pi f_c t\right)\cos e(t) - \sin\left(2\pi f_c t\right)\sin e(t)\right] \tag{5.2}$$

Assuming $e(t) \ll 1$, Eq. (5.2) can be approximated, as follows

$$y(t) \approx A_C[x(t) \times \cos\left(2\pi f_c t\right) - x(t)e(t) \times \sin\left(2\pi f_c t\right)] \tag{5.3}$$

As proved in Appendix C, the PSD of the baseband representation of the multiplied signal, $x(t) \times g(t)$, denoted by $S_Y(f)$, is derived to be

$$S_Y(f) = 2A_C \left[\underbrace{S_X(f) * S_\Phi(f)}_{S_{Y1}(f)} + \underbrace{S_X(f) * S_{sp}(f) + S_X(f)}_{S_{Y2}(f)}\right] \tag{5.4}$$

where $S_{Y1}(f)$ and $S_{Y2}(f)$ are the output PSDs due to the PLL phase noise and spurs, respectively. It is worth noting that $S_{Y2}(f)$ also contains the effect of the carrier tone. The factor of two in (5.4) is attributed to the combination of the mixers' outputs to produce the quadrature signal. Eq. (5.4) can be normalized by $2A_C$, as it has no effect on the relative OOBE level. Therefore, the forthcoming equations regarding the relative out-of-band emission levels are considered general and can be used for various types of digital modulation schemes such as PAM-2^M, QPSK, and 4^MQAM.

5.1 Baseband Signal Representation

Each digital bit can be represented by a pulse that is transmitted during a specific time interval. If the transmitted pulse (or its skirts) extends beyond its designated interval, it will interfere with neighboring pulses. This phenomenon, commonly known as intersymbol interference (ISI), causes errors in the received signal. The ISI, stemming from channel distortion or imperfect filtering, can introduce errors into the received signal. Therefore, the main goal of advanced transmission techniques incorporating digital modulation schemes, such as quadrature amplitude modulation (QAM) and pulse amplitude modulation (PAM) is to design pulses that minimize ISI and improve the transmission quality. Raised cosine pulse shaping is a common technique used in digital communications to shape transmitted signals into a specific form so as to minimize ISI. In the time domain, the raised-cosine pulse is expressed, as follows[27, 45]

$$p(t) = V_p \times \mathrm{sinc}\left(\frac{t}{T_b}\right) \times \frac{\cos(\frac{\pi\beta t}{T_b})}{1 - \frac{4\beta^2 t^2}{T_b^2}} \tag{5.5}$$

where V_p and β are amplitude and the roll-off factor of the pulse-shaped signal, respectively, and the signal exhibits zero amplitude at integer multiples of T_b. Accordingly, the Fourier

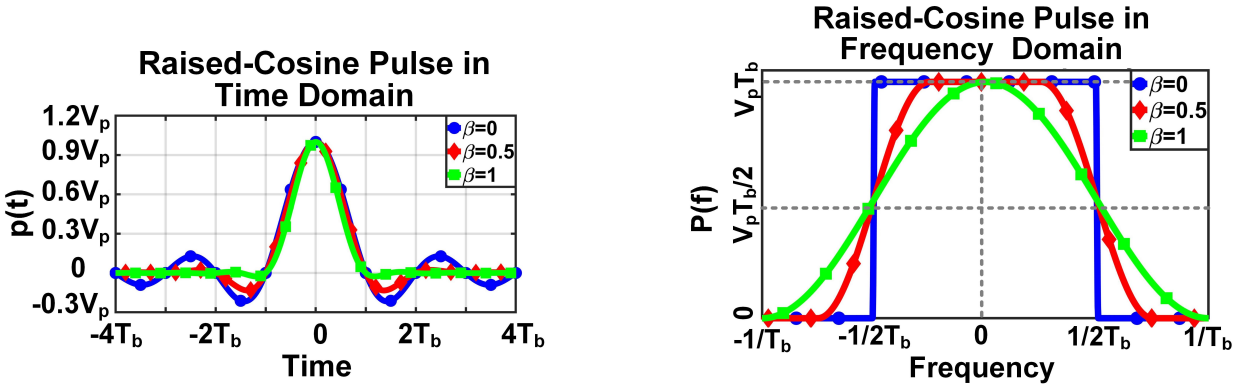

(a) (b)

Figure 5.2: Representation of a raised-cosine pulse in (a) time, and (b) frequency domain.

transform of a raised-cosine pulse is obtained, as follows [27]

$$P(f) = \begin{cases} V_p T_b & f < \frac{1-\beta}{2T_b} \\ \frac{V_p T_b}{2}\left[1+\cos\left[\frac{\pi T_b}{\beta}\left(f-\frac{1-\beta}{2T_b}\right)\right]\right] & \frac{1-\beta}{2T_b} \le f \le \frac{1+\beta}{2T_b} \\ 0 & f > \frac{1+\beta}{2T_b} \end{cases} \tag{5.6}$$

The temporal and spectral waveforms of the raised-cosine pulse are shown in Figs. 5.2a-5.2b, where the spectrum is confined within the bandwidth (defined to be the spectral width of the main lobe) of $\frac{1+\beta}{2T_b}$. For $\beta = 0$, which is abundantly used throughout this paper, Eq. (5.6) becomes:

$$P(f) = \begin{cases} V_p T_b & f < \frac{1}{2T_b} \\ 0 & f > \frac{1}{2T_b} \end{cases} \tag{5.7}$$

Suppose the baseband input, $x(t)$, takes the form of a PAM signal where the digital input stream, $b_k = \pm 1, \pm 3, \cdots, \pm(2^M - 1)$, directly modulate a raised-cosine pulse, $p(t)$, at a baud

rate of $1/T_b$, i.e.,

$$x(t) = \sum_k b_k p(t - kT_b) \tag{5.8}$$

With $P(f)$ satisfying Eq. (5.7), transmission with zero ISI is possible [14, 27]. It can be proved that if $b_k = \pm 1, \pm 3, \cdots, \pm(2^M - 1)$ occurs with equal probabilities, the power spectral density (PSD) of $x(t)$ is derived to be [4, 46, 47]

$$S_X(f) = \frac{\sigma_b^2}{T_b} |P(f)|^2 \tag{5.9}$$

where σ_b^2 is the variance of the input digital stream, which, for the case of a PAM-2^M signal, is calculated to be

$$\sigma_b^2 = \frac{4^M - 1}{3} \tag{5.10}$$

$S_X(f)$ for $\beta = 0$ is expressed as:

$$S_X(f) = \begin{cases} S_{BB} & f < f_{BB} \\ 0 & f > f_{BB} \end{cases} \tag{5.11}$$

where $f_{BB} = 1/2T_b$, and S_{BB} is defined as $S_{BB} = (4^M - 1)V_p^2 T_b/3$. Therefore, the total power P_X of the baseband signal is calculated to be:

$$P_X = \int_{-\infty}^{\infty} S_X(f) df = 2 S_{BB} f_{BB} = \frac{4^M - 1}{3} \times V_p^2 \tag{5.12}$$

Eqs. (5.11) and (5.12) are used throughout this paper as the PSD and total power of the input baseband signal, respectively.

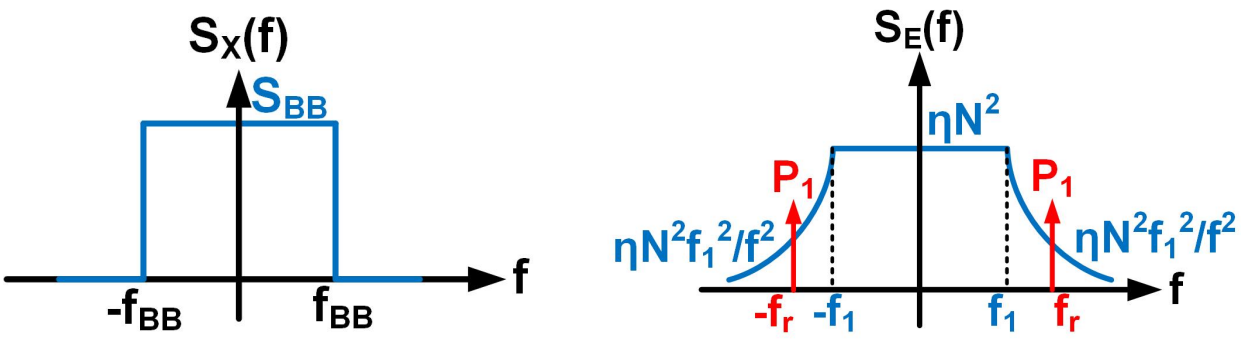

(a) (b)

Figure 5.3: The PSDs of (a) baseband signal, and (b) PLL phase noise.

5.2 Integer-N PLL Impact on OOBE

To accurately calculate the PSD of the mixer's output due to the PLL phase noise for a pulse-shaped random digital stream, Eqs. (5.9) and (2.6) must be convolved. However, a closed-form expression cannot be obtained. Intuitively, one can surmise that as the roll-off factor decreases, the signal bandwidth will reduce, which leads to an increase in OOBE. More precisely, the input PSD around the edges of the band (i.e., around $f = \pm\frac{1+\beta}{2T_b}$) increases, thus, producing a larger output PSD when convolving with the PLL spectrum for $|f| > \frac{1+\beta}{2T_b}$. Therefore, the worst-case OOBE occurs when $\beta = 0$. To capture the worst-case scenario, the input signal PSD, $S_X(f)$, is approximated by a rectangular spectrum whose PSD is expressed by (5.11) (*cf.* Fig. 5.3a). Additionally, $S_E(f)$, the spectrum of $e(t)$, is shown in Fig. 5.3b in which blue curve and red impulses denote phase noise and spurs, respectively. The PSD of the mixer's output $S_{Y1}(f)$ due to PLL phase noise is obtained approximately by convolving Eqs. (5.11) and (2.9), resulting in

$$\frac{S_{Y1}(f)}{S_{BB} \times N^2\eta} = \begin{cases} \frac{2f_1^2 f_{BB}}{f^2 - f_{BB}^2} & f \geq f_{BB} + f_1 \\ 2f_1 - \frac{(f^2 - f_{BB}^2 + f_1^2)}{f + f_{BB}} & \left|f - f_{max}\right| \leq f_{min} \\ 4f_1 + \frac{2f_1^2 f_{BB}}{f^2 - f_{BB}^2} & f \leq f_{BB} - f_1 \\ 2f_{BB} & f \leq f_1 - f_{BB} \end{cases} \tag{5.13}$$

where f_{max} and f_{min} are defined as $\max(f_1, f_{BB})$ and $\min(f_1, f_{BB})$, respectively. Furthermore, $S_{Y2}(f)$ is obtained by convolving Eqs. (5.11) and (2.24), and adding the baseband spectrum, $S_X(f)$, to the result, leading to:

$$S_{Y2}(f) = S_X(f) + P_1 S_X(f - f_r) + P_1 S_X(f + f_r) \tag{5.14}$$

In practice, for an integer-N PLL, the channel spacing is either the same or an integer multiple of the PLL reference frequency[4]. Therefore, $f_r \geq 2f_{BB}$, simplifying Eq. (5.14) to:

$$S_{Y2}(f) = \begin{cases} S_{BB} & f \leq f_{BB} \\ P_1 S_{BB} & \left|f - f_r\right| \leq f_{BB} \\ 0 & \text{Otherwise} \end{cases} \tag{5.15}$$

Referring to Eq. (5.4), the normalized PSD of the mixer's output, $S_Y(f)$, is obtained by adding Eqs. (5.13) and (5.15). In the special case where the PLL spurs are negligible, the normalized PSD for positive frequencies is approximately calculated by:

$$\frac{S_Y(f)}{S_Y(0)} \approx \begin{cases} 1 & f \leq f_{BB} \\ 2\eta N^2 f_{BB} & f_{BB} \leq f \leq f_1 - f_{BB} \\ \eta N^2 \left[2f_1 - \frac{(f^2 - f_{BB}^2 + f_1^2)}{f + f_{BB}}\right] & \left|f - f_{max}\right| \leq f_{min} \;\&\; f \geq f_{BB} \\ \eta N^2 \frac{2f_1^2 f_{BB}}{f^2 - f_{BB}^2} & f \geq f_{BB} + f_1 \end{cases} \tag{5.16}$$

It is inferred from Eq. (5.16) that decreasing f_1 will lower OOBE. This, in turn, implies that reducing the VCO phase noise or the PLL loop bandwidth through the reduction of R_1, K_{VCO}, or I_p can improve OOBE. Meanwhile, reducing R_1 will decrease ζ, making the PLL loop less stable. Therefore, one way of improving OOBE is to reduce K_{VCO} and I_p, while boosting R_1 with the same scaling factor so as to keep ζ constant, and thus, avoid degrading loop stability. This procedure, however, narrows the tuning range of both the VCO and the

PLL. It should also be noted that if the PLL loop bandwidth becomes excessively small, Eq. (2.9) cannot predict the PLL phase noise profile, accurately. Hence, Eq. (5.16) becomes inaccurate.

5.3 Fractional-N PLL Impact on OOBE

Similarly, for the fractional-N PLL, the mixer's output PSD due to PLL phase noise, $S_{Y1}(f)$, is derived by replacing every η in Eq. (2.6) with $S_I(f)$ in (2.42), and subsequently, convolving the result with Eq. (5.9). However, the resulting integration does not lead to a closed-form expression, and can only be calculated numerically. Similar to previous section, to obtain an insightful closed-form expression for the spectrum of the mixer's output due to PLL phase noise, Eq. (5.11) is convolved with Eq. (2.47), yielding:

$$\frac{S_{Y1}(f)}{S_{BB}} = \begin{cases} (\alpha + 4\zeta^2 f_n^2 S_R)\frac{2f_{BB}}{f^2 - f_{BB}^2} & f \geq f_{BB} + f_2 \\ (f_2 + f_{BB} - f)S_R + \lambda_L \frac{f_2^{2L-1} - (f - f_{BB})^{2L-1}}{2L-1} + (\alpha + 4\zeta^2 f_n^2 S_R)(\frac{1}{f_2} - \frac{1}{f + f_{BB}}) & \left|f - f_{max}\right| \leq f_{min} \\ (\alpha + 4\zeta^2 f_n^2 S_R)(\frac{2}{f_2} + \frac{2f_{BB}}{f^2 - f_{BB}^2}) + 2f_2 S_R + \lambda_L \frac{2f_2^{2L-1}}{2L-1} & f \leq f_{BB} - f_2 \\ 2f_{BB} S_R + \lambda_L \frac{(f + f_{BB})^{2L-1} - (f - f_{BB})^{2L-1}}{2L-1} & f \leq f_2 - f_{BB} \end{cases} \tag{5.17}$$

As mentioned earlier, the spur generation mechanism in a fractional-N PLL follows that in an integer-N counterpart. Consequently, Eq. (5.15) is used to express the mixer's output PSD due to PLL's spurs as well as the carrier tone. Therefore, the normalized PSD of the mixer's output, $S_Y(f)$, is obtained by adding Eqs. (5.15) and (5.17). For instance, in the case where the PLL spurs are negligible, the normalized PSD for positive frequencies is approximately

calculated, as:

$$\frac{S_Y(f)}{S_Y(0)} \approx \begin{cases} 1 & f \le f_{BB} \\ 2f_{BB}S_R + \lambda_L \frac{(f+f_{BB})^{2L-1} - (f-f_{BB})^{2L-1}}{2L-1} & f_{BB} \le f \le f_2 - f_{BB} \\ (f_2 + f_{BB} - f)S_R + \lambda_L \frac{f_2^{2L-1} - (f-f_{BB})^{2L-1}}{2L-1} + (\alpha + 4\zeta^2 f_n^2 S_R)(\frac{1}{f_2} - \frac{1}{f+f_{BB}}) & \left|f - f_{max}\right| \le f_{min} \ \& \ f \ge f_{BB} \\ (\alpha + 4\zeta^2 f_n^2 S_R)\frac{2f_{BB}}{f^2 - f_{BB}^2} & f \ge f_{BB} + f_2 \end{cases} \tag{5.18}$$

Eq. (5.18) suggests that a reduction in QNF and/or the PLL bandwidth directly lowers the OOBE level.

Chapter 6

The Effect of Circuit Nonlinearity & Bandwidth Limitation on EVM & OOBE

This chapter delves into an examination of how circuit nonlinearity and bandwidth limitations influence the performance parameters of a TRX, including EVM and OOBE.

6.1 The Effect of Circuit Nonlinearity & Bandwidth Limitation on OOBE

TX circuit blocks, especially those up the TX chain close to the antenna, exhibit nonlinearity that degrades the TX performance in terms of EVM [48]. Additionally, nonlinearity causes spectral regrowth, which elevates the OOBE level. PA, handling large signals, is arguably the most critical TX block in terms of nonlinearity. The PA nonlinearity can be captured

by Taylor's series approximation of its nonlinear input-output characteristic [4], as follows:

$$w(t) = \sum_{k=0}^{\infty} a_k \times y^k(t) \tag{6.1}$$

where a_k is an empirical coefficient describing the k^{th}-order nonlinearity of the PA, and $y(t)$ and $w(t)$ represent the PA's input and output signals, respectively. Approximating Eq. (6.1) with its first four terms where a_0 is the output's DC voltage, a_1 is the linear voltage gain of the system, and a_2 and a_3 are the second- and third-order nonlinearity coefficients, respectively, leads to [4]

$$V_{out}(t) = V_{DC} + A_V V_{in}(t) + \frac{2A_V}{A_{IIP2}} V_{in}^2(t) + \frac{4A_V}{3A_{IIP3}^2} V_{in}^3(t) \tag{6.2}$$

The second-order nonlinearity is significantly reduced by adopting fully-differential signaling. Disregarding the DC and second-order terms, the power-series is simplified to

$$V_{out}(t) = A_V V_{in}(t) + \frac{4A_V}{3V_{IIP3}^2} V_{in}^3(t) \tag{6.3}$$

Moreover, with the input being a zero-mean random process, the output PSD is related to the input PSD, as follows[49]

$$\begin{aligned} S_W(f) = G_P \Bigg[& \left(1 + \frac{8P_Y}{3P_{IIP3}}\right) S_Y(f) \\ & + \frac{16}{9P_{IIP3}^2} [S_Y(f) * S_Y(f) * S_Y(f)] \Bigg] \end{aligned} \tag{6.4}$$

where P_Y is the total signal power that is fed to the PA, $G_P = A_V^2$ is the PA's available power gain, $P_{IIP3} = V_{IIP3}^2$, and $S_Y(f)$ and $S_W(f)$ are the PSD of input and output signals, respectively. P_Y is readily obtained to be $P_Y = 2 \times G_{MX} \times P_X$ where G_{MX} is the power gain of the mixer, and the factor of two arises due to combination of two quadrature signals after the mixers. It is noteworthy that Eq. (6.4) is not specific to the PA nonlinearity. In fact,

this equation can express the output PSD of an entire system consisting of cascaded blocks if G_P and P_{IIP3} denote the system's power gain and IIP3, respectively.

In a conventional TX chain, the PA is fed by the signal emerging from the output of the power combiner (*cf.* Fig. 5.1), where the two quadrature upconverted PAM signals are combined. Therefore, $S_Y(f)$, calculated in the preceding section, is the PA input PSD, which can be used in Eq. (6.4) to calculate the PA output PSD. However, the closed-form expression for this case cannot be obtained, necessitating numerical calculations. To address this issue, it is assumed that the PA is fed by the modulated PAM signal which is up-converted to the carrier frequency using a noiseless LO. This assumption enables us to obtain a closed-form expression for the PA output PSD. Additionally, it allows a comparison between the contributions of PLL phase noise and circuit nonlinearity to OOBE. Using Eq. (5.11) as the PA input signal's PSD, the output PSD, based on Eq. (6.4), is derived to be

$$\frac{S_W(f)}{G_P S_{BB}} = \begin{cases} -\frac{4P_X^2}{9P_{IIP3}^2}\left(\frac{f}{f_{BB}}\right)^2 + \frac{4(P_X+P_{IIP3})^2 - P_{IIP3}^2}{3P_{IIP3}^2} & f \le f_{BB} \\ \frac{2P_X^2}{9P_{IIP3}^2}\left(3 - \frac{f}{f_{BB}}\right)^2 & f_{BB} \le f \le 3f_{BB} \\ 0 & f \ge 3f_{BB} \end{cases} \tag{6.5}$$

PAs having multiple stages are ubiquitously used in high-frequency (e.g., mm-wave and THz) TX architectures, where each stage has an L-C resonant circuit filtering the output signal. For instance, Fig. 6.1 illustrates a PA incorporating k stages each having a second-order band-pass filter (BPF). Therefore, the overall PA circuit uses a $2k^{\text{th}}$-order BPF. Assuming each stage of filtering has the same center frequency of f_c and quality factor of Q, the normalized magnitude of the transfer function of each filtering stage is derived to be

$$\frac{|H(f)|}{|H(f_c)|} \approx \frac{1}{\sqrt{1 + Q^2\left(1 - \frac{f^2}{f_c^2}\right)^2}} \tag{6.6}$$

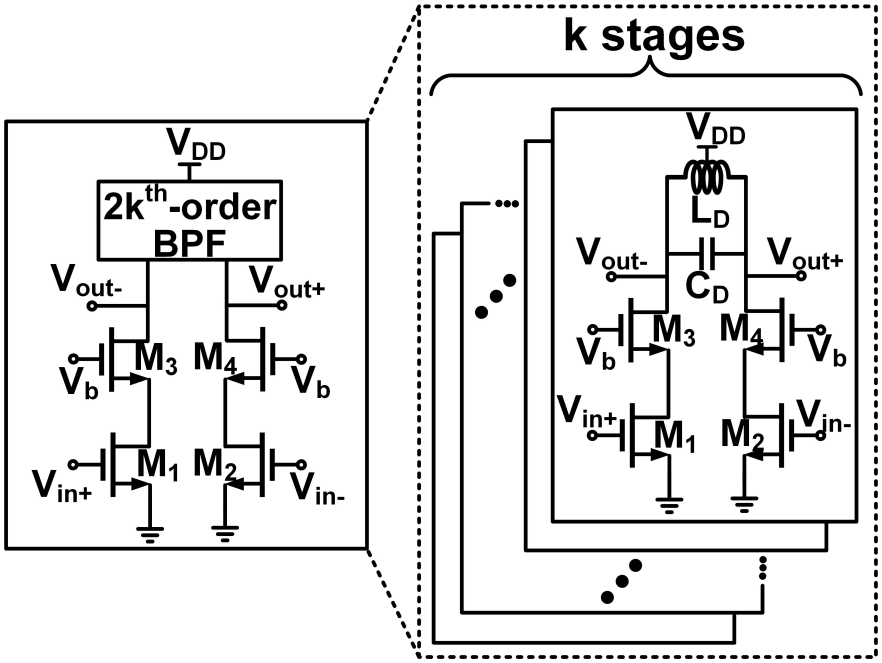

Figure 6.1: A multi-stage power amplifier circuit model.

where $f_c = 1/2\pi\sqrt{L_D C_D}$, and L_D and C_D are the inductor and capacitor values, respectively [50]. For frequencies close to f_c (i.e., $0.9f_c < f < 1.1f_c$), Eq. (6.6) is approximated by

$$\frac{|H(f)|}{|H(f_c)|} \approx \frac{1}{\sqrt{1 + \frac{4Q^2}{f_c^2}\Delta f^2}} \tag{6.7}$$

where Δf is the offset frequency from the center frequency, f_c. Therefore, Taking into account for the PA bandwidth, the baseband representation of the output signal spectrum is:

$$S_Z(f) = \frac{S_W(f)}{\left|1 + \frac{4Q^2}{f_c^2} f^2\right|^k} \tag{6.8}$$

where $S_W(f)$, the PA's output PSD disregarding its limited bandwidth, was calculated in

Eq. (6.5). The normalized PSD of the PA output for positive frequencies is obtained in:

$$\frac{S_Z(f)}{S_Z(0)} = \frac{1}{\left|1+\frac{4Q^2}{f_c^2}f^2\right|^k} \times \begin{cases} 1 - \frac{\frac{4}{3}P_X^2}{4(P_X+P_{IIP3})^2 - P_{IIP3}^2} \times \left(\frac{f}{f_{BB}}\right)^2 & f \le f_{BB} \\ \frac{\frac{2}{3}P_X^2}{4(P_X+P_{IIP3})^2 - P_{IIP3}^2} \times \left(3 - \frac{f}{f_{BB}}\right)^2 & f_{BB} \le f \le 3f_{BB} \\ 0 & f \ge 3f_{BB} \end{cases} \quad (6.9)$$

It is observed that linearizing the PA (i.e., increasing P_{IIP3}) and increasing the order and quality factor of the filter reduces OOBE, especially at larger offset frequencies.

6.2 The Effect of Circuit Nonlinearity & Bandwidth Limitation on EVM

It is widely known that the PA non-linearity leads to amplitude compression whose detrimental effect is exacerbated when dealing with envelope-variable modulation schemes such as high-order QAM[4]. To quantify this performance degradation, the EVM due to PA non-linearity is calculated. Prior work analyzed nonlinearity-induced constellation distortion and EVM degradation using a polynomial model for the PA [51]. In this work, PA non-linearity is modeled using the method introduced in [52] that relates the PA output's phase shift and amplitude to the input amplitude. Suppose that the modulated input signal is expressed as $x(t) = a(t)\cos[\omega_0 t + \phi(t)]$. The PA's output waveform becomes $y(t) = A(a(t))\cos[\omega_0 t + \phi(t) + \Theta(a(t))]$ where $A(t)$ and $\Theta(t)$ capture the "AM/AM conversion" and "AM/PM conversion", respectively, and both are functions of the input signal's amplitude, $a(t)$, i.e.,

$$A(a(t)) = \frac{\alpha_1 a(t)}{1+\beta_1 a^2(t)} \quad (6.10)$$

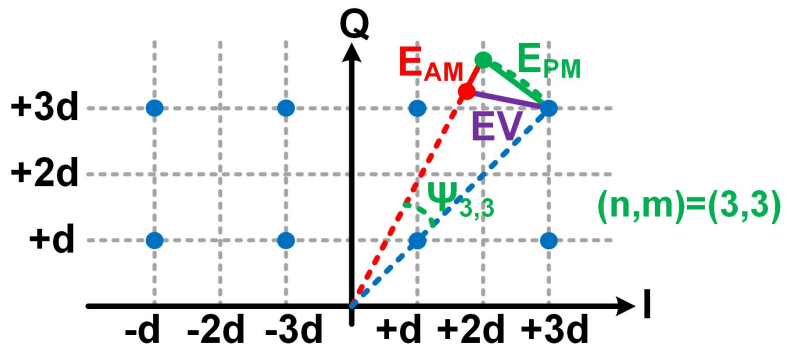

Figure 6.2: QAM constellation undergoing PA AM/AM and AM/PM distortions.

$$\Theta\left(a\left(t\right)\right) = \frac{\alpha_2 a^2\left(t\right)}{1+\beta_2 a^2\left(t\right)} \tag{6.11}$$

where $\alpha_1, \alpha_2, \beta_1$, and β_2 are empirical fitting parameters[4].

PA non-linearity causes the transmitted symbols to deviate from the ideal ones in the constellation diagram in two different ways: (1) AM/PM conversion acts as a phase shift rotating the symbols around the origin of the constellation diagram, while maintaining a fixed distance from the origin. (2) AM/AM conversion changes the radial distance of the rotated symbols from the origin. These effects are shown in Fig. 6.2 for only one of the QAM symbols for the sake of clarity.

In a conventional transmitter generating 4^MQAM symbols in the digital domain, each symbol has its own error vector (EV) determined by the symbol power (i.e., the square of the distance from the origin of the constellation diagram). $EV_{n,m}$ is defined to be the EV associated with symbol $(I,Q) = (n,m)$. Therefore, EVM is obtained to be

$$EVM = \sqrt{\frac{\frac{1}{4^{M-1}} \sum_{\substack{n=1,\\ n\in\text{odd}}}^{2^M-1} \sum_{\substack{m=1,\\ m\in\text{odd}}}^{2^M-1} EV_{n,m}^2}{ASP}} \tag{6.12}$$

where n and m are odd numbers (i.e., $n, m = 2l - 1$ where $l \in \mathbb{N}$), ASP denotes the average symbol power, and M is the order of modulation. The following steps are taken to calculate EVM: (1) the ASP of the transmitted constellation diagram as well as the average rotation angle of all QAM symbols are calculated. Next, a perfect 4^MQAM constellation with no impairment is considered, which is rotated by this average rotation angle to obtain a reference constellation with a symbol-to-symbol spacing of $2d$. Furthermore, d is calculated such that the transmitted and the reference constellation ASPs are equal. (2) The effective phase difference between the two symbols in the transmitted and the corresponding reference constellation diagrams, $\psi_{n,m}$, is calculated (Fig. 6.2). (3) Using d and $\psi_{n,m}$, EV for each symbol in a 4^MQAM constellation diagram is derived and EVM is calculated, accordingly.

The PA input-signal amplitude during the transmission of symbol $(I, Q) = (n, m)$ within the 4^MQAM constellation is denoted by $a_{n,m} = a_u \times \sqrt{n^2 + m^2}$, where a_u is the unit amplitude. The average symbol power, ASP, of the distorted constellation diagram is derived to be:

$$ASP = \frac{1}{4^{M-1}} \sum_{n \in \text{odd}}^{2^M - 1} \sum_{m \in \text{odd}}^{2^M - 1} SP_{n,m} \tag{6.13}$$

where $SP_{n,m}$, the power of the distorted symbol $(I, Q) = (n, m)$ at the PA output, is

$$SP_{n,m} = \frac{\alpha_1^2 a_u^2 \left(n^2 + m^2\right)}{\left[1 + \beta_1 a_u^2 \left(n^2 + m^2\right)\right]^2} \tag{6.14}$$

As previously stated, the reference constellation is adjusted in two ways: (1) it is scaled by changing the minimum symbol-to-symbol spacing to match the transmitted average symbol power obtained in Eq. (6.13); (2) it is rotated by the average rotation angle of all constellation points, θ_{avg}, derived in Appendix D. Additionally, ASP of the reference constellation (assuming $2d$ symbol-to-symbol spacing) is calculated to be

$$ASP = \frac{2}{3} \times \left(4^M - 1\right) d^2 \tag{6.15}$$

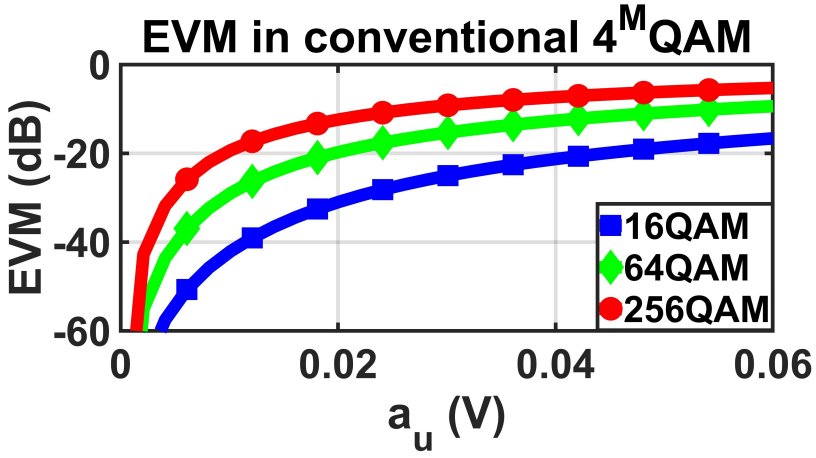

Figure 6.3: EVM due to PA AM/AM and AM/PM conversions.

The derivation steps to calculate d are found in Appendix D. $EV_{n,m}$ caused by AM/AM and AM/PM conversions is calculated to be:

$$EV_{n,m}^2 = E_{P_{n,m}}^2 + E_{A_{n,m}}^2 - 2E_{P_{n,m}}E_{A_{n,m}} \sin\frac{\psi_{n,m}}{2} \tag{6.16}$$

where $E_{P_{n,m}}$ and $E_{A_{n,m}}$ represent EVs of symbol $(I,Q) = (n,m)$ generated by the AM/PM and AM/AM conversions, respectively, which are derived to be

$$E_{P_{n,m}} = 2d_{n,m} \sin\frac{\psi_{n,m}}{2} \tag{6.17}$$

$$E_{A_{n,m}} = d_{n,m} - \frac{\alpha_1 a_{n,m}}{1+\beta_1 a_{n,m}^2} \tag{6.18}$$

where $\psi_{n,m}$ is the effective phase difference between the transmitted $(I,Q) = (n,m)$ symbol and its associated reference constellation point. Moreover, $d_{n,m}$ is the distance of $(I,Q) = (n,m)$ symbol in the reference constellation to the origin. These two parameters are calculated in Appendix D.

Using Eqs. (6.12)-(6.14), and (6.16), the EVM of a conventional transmitter handling

4^MQAM is derived, as follows

$$EVM = \sqrt{\frac{\sum_{n\in\text{odd}}^{2^M-1}\sum_{m\in\text{odd}}^{2^M-1} E_{P_{n,m}}^2 + E_{A_{n,m}}^2 - 2E_{P_{n,m}}E_{A_{n,m}}\sin\frac{\psi_{n,m}}{2}}{\sum_{n\in\text{odd}}^{2^{M-1}}\sum_{m\in\text{odd}}^{2^{M-1}} SP_{n,m}}} \tag{6.19}$$

A CMOS 125-GHz PA, whose topology and design specifications will be disclosed in subsequent chapters, is considered. The circuit-simulated fitting parameters capturing the PA non-linearity are $\alpha_1 = 8.34,\ \beta_1 = 10.47,\ \alpha_2 = 11.18,$ and $\beta_2 = 19.67$. Fig. 6.3 shows the plots of EVM as calculated by Eq. (6.19) for three modulation schemes, namely, 16QAM, 64QAM, and 256QAM. It is observed that EVM is degraded as the PA input amplitude grows. Additionally, the rate of this degradation increases with the modulation order.

The limited bandwidth of PA and DAC as well as other blocks contribute to intersymbol interference (ISI). In a conventional 4^MQAM architecture, a non-zero EV is generated due to the unsettled transition from one symbol to another because of the transmitter's limited bandwidth. Taking a similar approach to [53], for 4^MQAM, the EV's probability density function (PDF) of in-phase and quadrature components are

$$P_{|EV_I|}(x) = P_{|EV_Q|}(x) = \begin{cases} \frac{1}{\epsilon} & -\frac{\epsilon}{2} < x < \frac{\epsilon}{2} \\ 0 & \text{otherwise} \end{cases} \tag{6.20}$$

where $\epsilon = (2^M - 1)\times 2d\exp(-\frac{2\pi\times BW_{TX}}{f_{BB}})$, and BW_{TX} and f_{BB} are the transmitter's low-pass-equivalent bandwidth and the baseband symbol rate, respectively. Therefore, the average EV power is readily obtained:

$$\overline{|EV|^2} = 2\int_{-\frac{\epsilon}{2}}^{+\frac{\epsilon}{2}} x^2 \times \frac{1}{\epsilon}\,dx = \frac{\epsilon^2}{6} \tag{6.21}$$

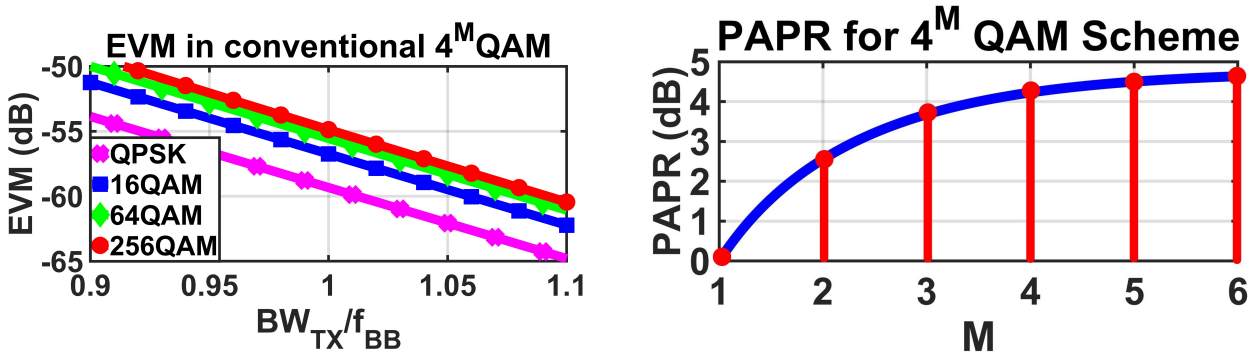

(a) (b)

Figure 6.4: (a) EVM due to bandwidth limitation for QPSK, 16QAM, 64QAM, and 256QAM schemes in a conventional transmitter. (b) PAPR of a 4^MQAM signal.

Additionally, ASP of the reference constellation is derived as

$$ASP = \frac{2}{3} \times \left(4^M - 1\right) \times \left(d - \frac{\epsilon}{2}\right)^2 \tag{6.22}$$

Hence,

$$EVM_{4^MQAM} = \sqrt{1 - \frac{2}{2^M + 1}} \times \frac{e^{-2\pi \frac{BW_{TX}}{f_{BB}}}}{1 - \left(2^M - 1\right) e^{-2\pi \frac{BW_{TX}}{f_{BB}}}} \tag{6.23}$$

Fig. 6.4a shows the plot of Eq. (6.23) for QPSK and three different QAM schemes (i.e., 16QAM, 64QAM, and 256QAM). It is observed that EVM induced by the transmitter's limited bandwidth increases with the modulation order.

Chapter 7

Simulation Results

The simulation results verifying the results obtained in the previous sections are presented, here.

7.1 PLL Phase Noise Impact on BER & EVM

To accurately assess the impact of PLL jitter and the link AWGN on BER and EVM, the behavioral model of the entire communication link was built in MATLAB. In this model, the random data with 1 GSamples/sec data rate was first generated by a pseudo-random bit sequence (PRBS) generator to obtain 9×10^4 samples (limited by maximum available storage space of our computing infrastructure). After being modulated by a digital modulator, the signal was upconverted by a mixer to 28-GHz RF frequency, then passed through an AWGN channel following the power amplification. The channel output was amplified and then downconverted by an LNA and a mixer, respectively, where the mixer was fed by an integer-N PLL-based LO. Next, a 4-th order LPF filtered the out-of-band frequency components. Finally, the filter's output went through a demodulator, where the bit stream was extracted.

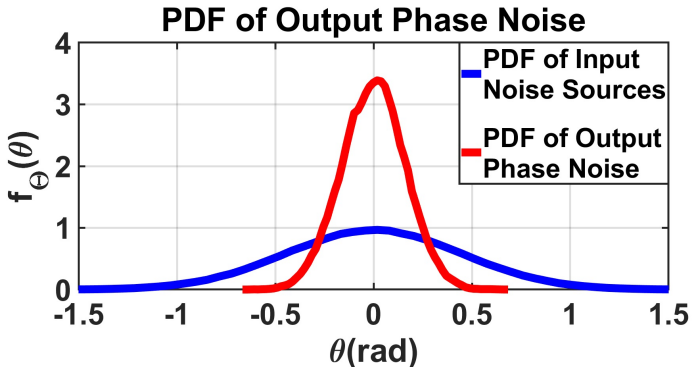

Figure 7.1: Simulated probability density functions of the PLL input and output noise.

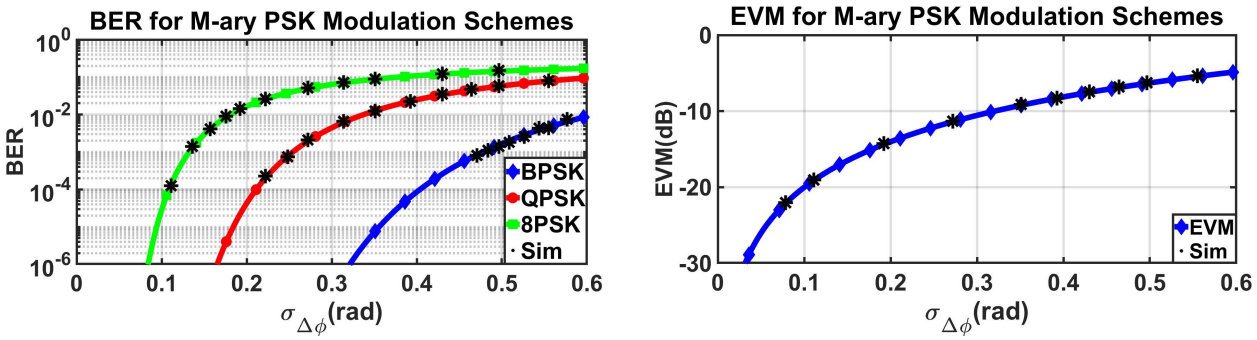

(a) (b)

Figure 7.2: (a) Simulated and estimated BERs for M-ary PSK modulation scheme. (b) Simulated and estimated EVMs for M-ary PSK modulation scheme.

As part of this behavioral model, a 28-GHz integer-N PLL with $I_P = 1$ mA, $R_1 = 4.7$ kΩ, $C_1 = 17$ pF, $K_{VCO} = 2\pi \times 3$-GHz/V, $N = 280$, and 100-MHz input frequency was developed. Based on these specifications, the loop dynamic parameters are $\zeta = 1$ and $\omega_n = 2\pi \times 4$-MHz. Fig. 7.1 shows the simulated PDF of the PLL phase noise due to the VCO and input noise using the aforementioned parameters. This simulation confirms that the PDF of the PLL phase noise remains Gaussian for a Gaussian-distributed input noise. Moreover, the entire link was simulated for $\rho_s, \rho_{min} = 10$, $\rho_s, \rho_{min} = 13$, and $\rho_s, \rho_{min} = 16$ dB.

As the first experiment, the standalone PLL was simulated using the above simulation setup and in the case of $\eta = 10^{-14}$ V^2/Hz. Next, to examine the accuracy of the proposed BER and EVM analytical models, the simulation was conducted for two cases, namely, (1) the only source of noise in the transceiver chain was the PLL phase noise on the receiver side,

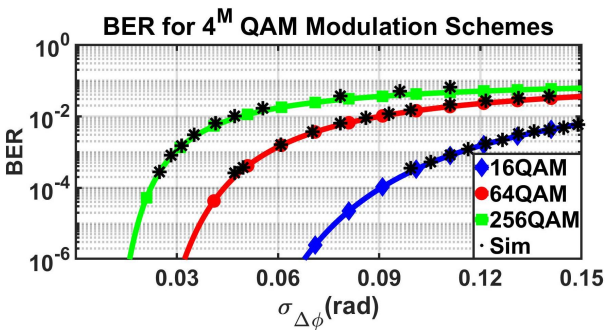

(a)

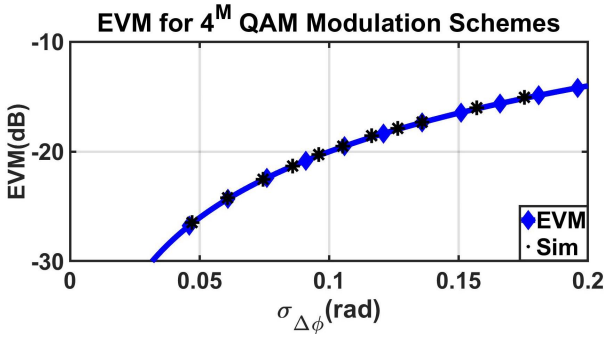

(b)

Figure 7.3: (a) Simulated and estimated BERs for 4^MQAM scheme. (b) Simulated and estimated EVMs for 4^MQAM scheme.

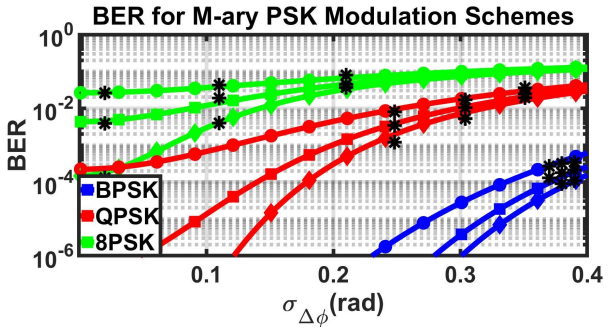

(a)

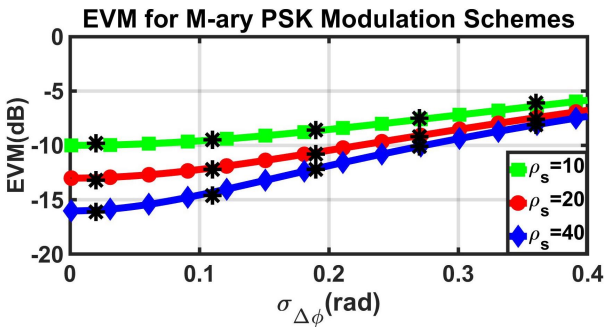

(b)

Figure 7.4: (a) Simulated and estimated BERs for M-ary PSK modulation scheme. (b) Simulated and estimated EVMs for M-ary PSK modulation scheme.

and (2) both PLL phase noise and the link AWGN were present.

In case of no link AWGN, Figs. 7.2a and 7.2b demonstrate BER and EVM variations with respect to RMS phase jitter for M-ary PSK modulation schemes, respectively. A comparison between the BER plots derived from Eqs. (3.4) and (3.12) (solid lines) and the ones obtained from MATLAB simulation (black asterisks) confirms the same variation trend between the two. Moreover, Figs. 7.3a and 7.3b show plots of simulated BER and EVM versus RMS phase jitter for 4^MQAM scheme. Indicated on the same figures are the estimated BER and EVM versus RMS phase jitter from Eqs. (4.13) and (4.19).

As for the second case, when both PLL jitter and link AWGN are taken into consideration, Figs. 7.4a and 7.4b demonstrate BER and EVM variations predicted by both analytical

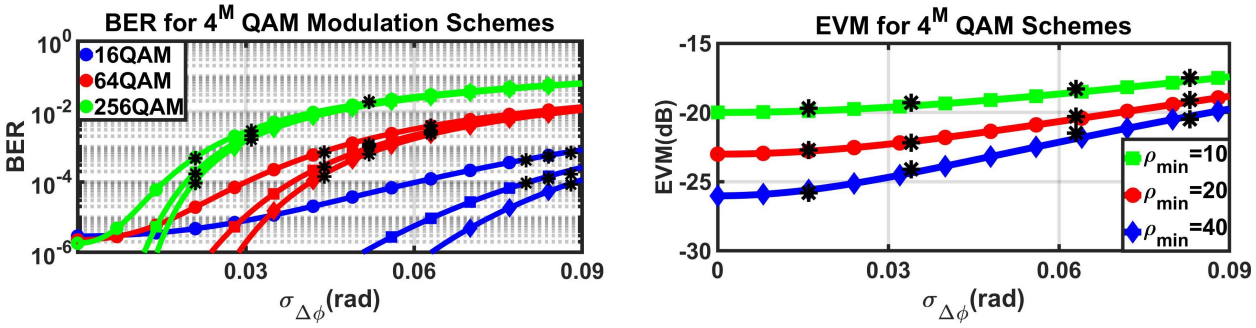

(a) (b)

Figure 7.5: (a) Simulated and estimated BERs for 4^MQAM scheme. (b) Simulated and estimated EVMs for 4^MQAM scheme.

models (Eqs. (3.4) and (3.21)) and MATLAB simulations for three distinct values of ρ_s with respect to RMS phase jitter for M-ary PSK modulation schemes (BPSK, QPSK, and 8PSK), respectively. Moreover, Figs. 7.5a and 7.5b, once again, show plots of BER and EVM based on analysis (Eqs. (4.17) and (4.20)) and MATLAB simulations for three different 4^MQAM schemes (16QAM, 64QAM, 256QAM) and $\rho_{min} = 10, 13, 16$ dB. A closer look at all the above BER and EVM plots shows similar trends for BER and EVM variations with respect to LO phase jitter for all modulations under consideration in this work.

7.2 PLL Phase Noise Impact on OOBE

To examine the accuracy of the proposed analytical study, comprehensive system-level simulations have been performed, and the important results are presented, here.

7.2.1 Baseband

A raised-cosine pulse-shaped PAM-4 signal with a baud rate of 100 MS/s was used as baseband digital stream. The roll-off factor was considered to be $\beta = 0$. Fig. 7.6a shows the simulated baseband PAM-4 signal with a minimum amplitude of 100 mV. Fig. 7.6b displays

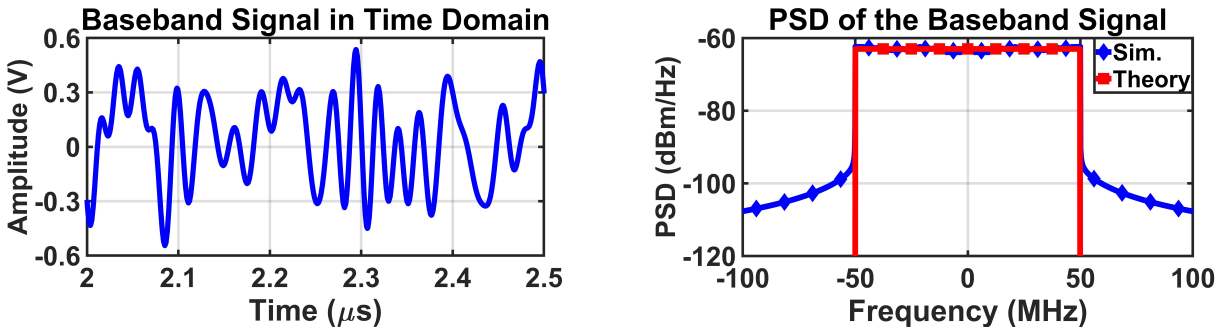

(a) (b)

Figure 7.6: Representation of the baseband signal in (a) time, and (b) frequency domain.

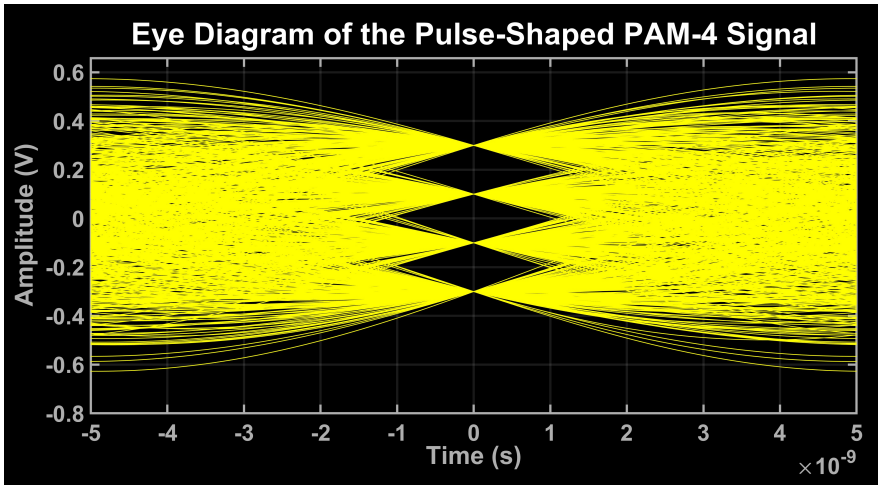

Figure 7.7: Eye diagram of the pulse-shaped PAM-4 signal.

a comparison between the PSDs of the baseband signal acquired from simulation (in red squares) and closed-form expression in (5.11) (in blue diamonds), where these results follow one another with 1-dB accuracy within the signal's bandwidth. The out-of-band PSD of the simulated baseband signal is more than 40 dB weaker than the in-band PSD. The discrepancy between analysis and simulation results is attributed to the limited number of simulated symbols (i.e., 800 symbols), which is imposed by the finite storage capacity of our computational infrastructure. Furthermore, the simulated eye diagram of the transmitted baseband signal is shown in Fig. 7.7, where the horizontal and vertical eye-openings for the simulated 800 symbols are around 2 ns and 200 mV, respectively.

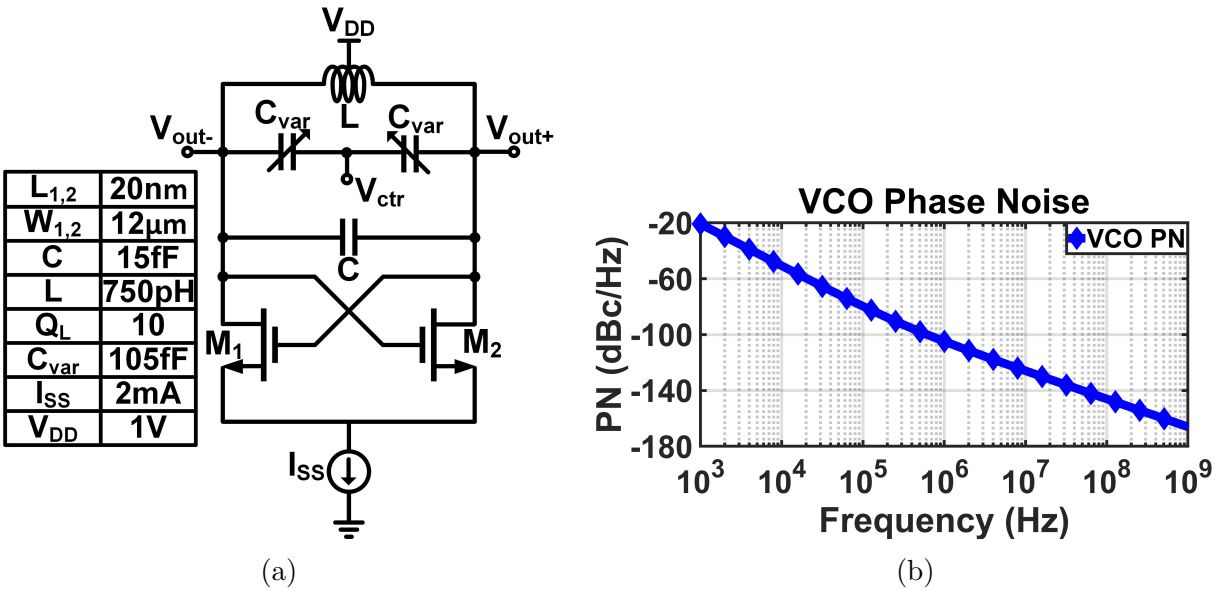

(a) (b)

Figure 7.8: The simulated VCO (a) schematic, and (b) phase noise profile.

7.2.2 Integer-N Frequency Synthesizer

A behavioral model of a type-II integer-N PLL was constructed in MATLAB. The PLL loop parameters were chosen, as follows: I_P = 1 mA, R_1 = 6 kΩ, C_1 = 30 pF, and N = 280. The reference was a 100 MHz crystal oscillator with a flat phase noise profile at –160 dBc/Hz. The constituent VCO, oscillating at the center frequency of 28 GHz, employed a varactor-based LC cross-coupled pair topology with K_{VCO} = 4GHz/V (*c.f.* Fig. 7.8a), and was designed and simulated in a 22nm CMOS process. At 2-mW of DC power, the VCO exhibited a simulated phase noise of –105 dBc/Hz at 1 MHz offset and a $1/f^3$ corner frequency of 330 kHz. Fig. 7.8b shows the phase noise profile, from which α = 12.5 and γ = 4.13×10^6. Consequently, the damping factor, natural frequency, and loop bandwidth of this PLL are calculated to be 1.96, 3.47 MHz, and 13.6 MHz, respectively. The resulting red squares in Fig. 7.9 represent the PLL output phase-noise profile, while, the green circles and blue diamonds depict the exact and approximate expressions calculated in Eqs. (2.6) and (2.47), respectively. It is evident that the approximate phase noise expression derived for an integer-N PLL in Eq. (2.47) accurately tracks the actual simulated counterpart.

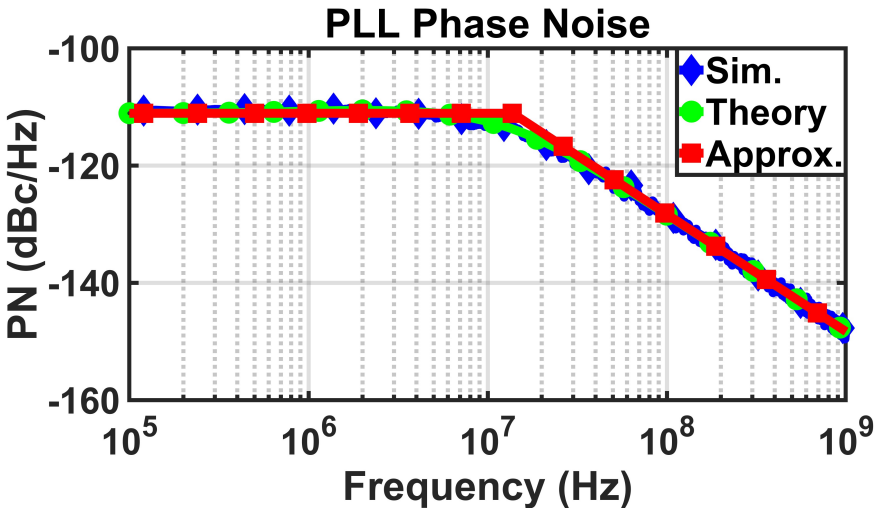

Figure 7.9: Simulated and estimated integer-N PLL phase noise.

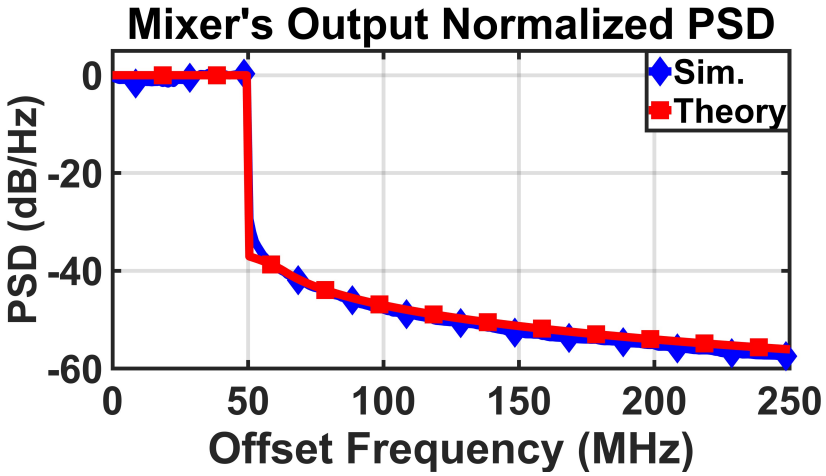

Figure 7.10: Normalized mixer's output PSD for the case of integer-N PLL.

To up-convert the baseband signal, a mixer driven by the PLL with a conversion gain of 3 dB was employed. Fig. 7.10 illustrates the normalized PSD of the mixer's output versus offset frequency from the carrier. The simulated results are represented by the blue diamonds, whereas the red squares represent the PSD derived from the proposed theoretical framework. Comparing the simulated results with the theoretical expressions demonstrates the accuracy of the theoretical derivations.

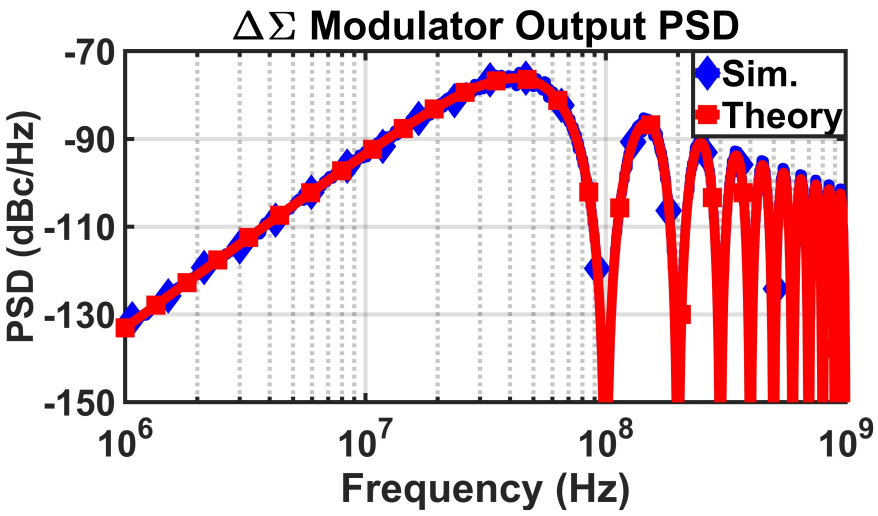

Figure 7.11: Simulated and calculated $\Delta\Sigma$ modulator output PSD.

7.2.3 Fractional-N Frequency Synthesizer

A behavioral model of a type-II fractional-N PLL was simulated in MATLAB. The PLL loop parameters including the charge pump current and VCO gain were kept the same as those used for the integer-N PLL. Additionally, a $\Delta\Sigma$ modulator was employed to vary the division ratio of the feedback path such that the average division ratio was 280.2, resulting in a 28.02 GHz output signal from a 100 MHz reference clock. The $\Delta\Sigma$ modulator and fractional-N PLL models used in these simulations were obtained from [54], which provided a comprehensive PLL model considering the effects of instantaneous division ratio variations.

A second-order $\Delta\Sigma$ modulator was utilized to generate a random binary sequence that averaged to 0.2, while shaping the phase noise profile. The shaped quantization noise PSD of the $\Delta\Sigma$ modulator, expected to have minimal power at low frequencies, is depicted in Fig. 7.11 using blue diamonds. In the same figure, Eq. (2.40) is also plotted using red squares. Additionally, the phase noise of the fractional-N PLL was analyzed in Fig. 7.12a.

The baseband signal was up-converted using the previously mentioned mixer. Fig. 7.12b

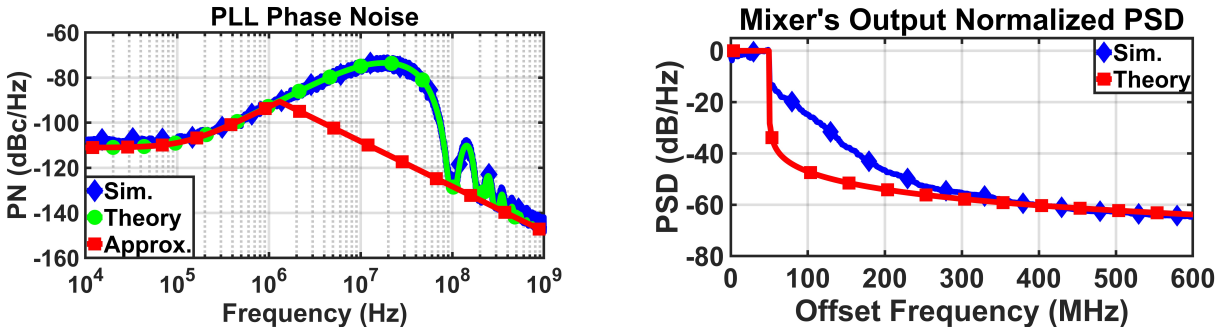

(a) (b)

Figure 7.12: (a) Simulated and estimated Fractional-N PLL phase noise. (b) Normalized mixer's output PSD for the case of fractional-N frequency synthesizer.

displays the normalized PSD of the mixer's output versus offset frequency from the carrier tone. The blue diamonds represent the simulation results, while the red squares depict the PSD derived from the theory developed throughout this paper.

7.3 Circuit Nonlinearity Impact on EVM & OOBE

This section presents the simulation results showing the impact of circuit nonlinearity on EVM and OOBE.

7.3.1 Circuit Nonlinearity Impact on EVM

To assess the impact of circuit nonlinearity on EVM, a two-stage class-AB PA with transformer-based matching [55]. The following fitting parameters were extracted to be used in MATLAB as PA behavioral model: $\alpha_1 = 8.34,\ \beta_1 = 10.47,\ \alpha_2 = 11.18,$ and $\beta_2 = 19.67$. AM/AM and AM/PM characteristics of the simulated PA are shown in Figs. 7.13a-7.13b in terms of the input power, P_{in}, referenced to 50 Ω. It is seen that for the low input power regime (e.g., ≤ –20 dBm) where the transfer characteristic remains linear, the distortion due to AM/AM and AM/PM conversions is negligible. The saturated output power of the PA was 12.2 dBm at

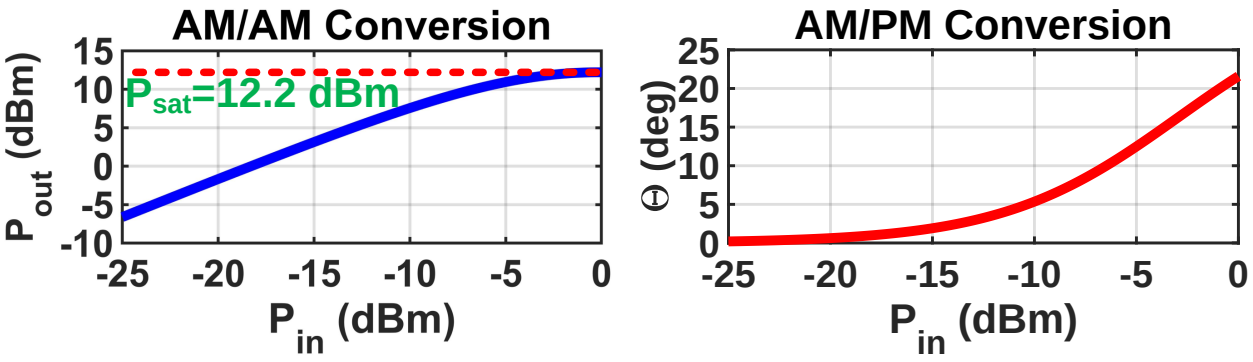

(a) (b)

Figure 7.13: (a) AM/AM and (b) AM/PM conversion characteristics of the simulated PA in terms of input power.

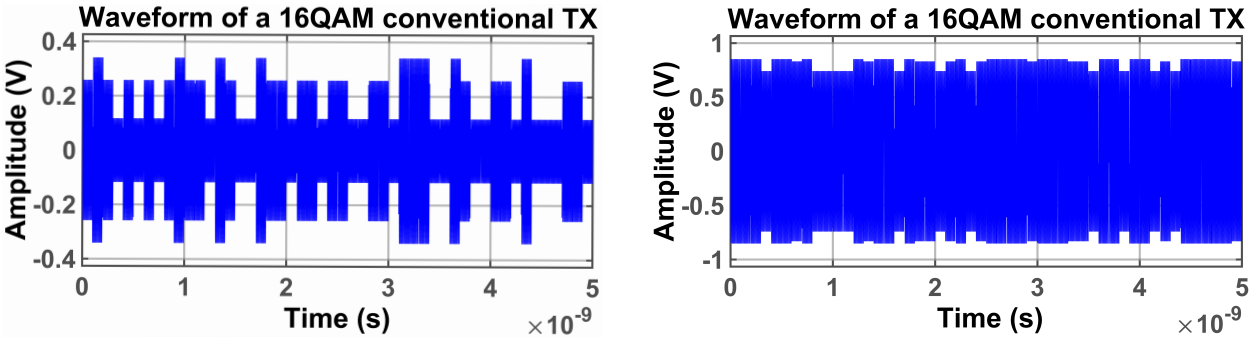

(a) (b)

Figure 7.14: Output waveform of a conventional transmitter incorporating 16QAM for (a) low, and (b) high input amplitudes.

an input of around 0 dBm. The designed PA was used in the conventional transmitter. The 16QAM waveform at the output of the PA is shown in Figs. 7.14a and 7.14b for low input amplitude (i.e., a_u =10 mV) and high input amplitude (i.e., a_u =100 mV), respectively. It is observed that when the input amplitude of the PA grows, due to its nonlinear characteristic, different symbols at the output become indistinguishable. Additionally, Fig. 7.15 shows the plot of EVM based on the developed analysis (i.e., Eq. (6.19)) and MATLAB simulations for three different 4^MQAM schemes, namely, 16QAM, 64QAM, and 256QAM. A comparison between the EVM plots derived from Eq. (6.19) (solid lines) and the ones obtained from MATLAB simulations (black asterisks) verifies the same variation trend between the two.

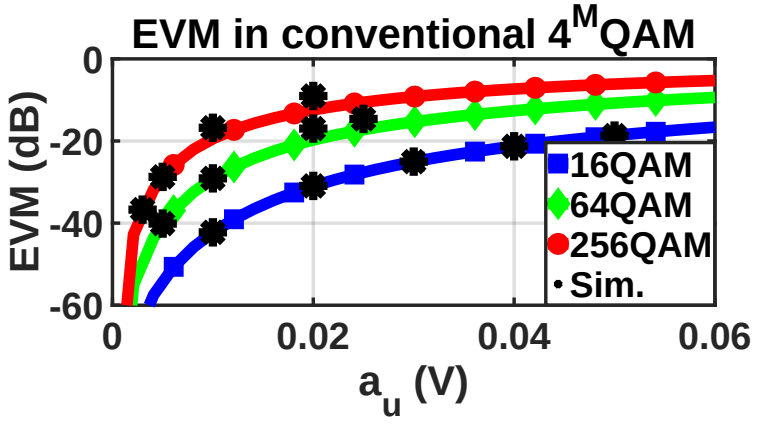

Figure 7.15: Theory-based and simulated EVM due to PA AM/AM and AM/PM conversions for 16QAM, 64QAM, and 256QAM in a conventional transmitter.

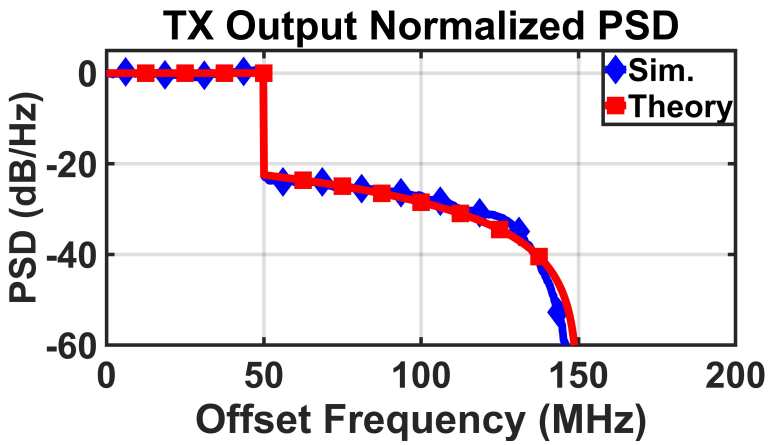

Figure 7.16: Normalized TX output PSD.

7.3.2 Circuit Nonlinearity Impact on OOBE

To evaluate the impact of circuit nonlinearity on OOBE, a behavioral model for the TX was developed. The TX chain has a gain of 20 dB and an IIP3 of 7.5 dBm. Fig. 7.16 depicts the normalized PSD of the TX's output signal at various offset frequencies. In this figure, the simulation results are represented by the blue diamonds, while the red squares depict the PSD derived from Eq. (6.5), which is based on the theoretical framework developed in this study. By comparing Figs. 7.10, 7.12b, and 7.16, it becomes apparent that the circuit nonlinearity affects OOBE at low offset frequencies. On the other hand, the PLL phase noise can potentially have a more detrimental impact at higher offset frequencies.

Bibliography

[1] Mohammad Oveisi, Huan Wang, and Payam Heydari. A Comparative Study of RF-QAM and Conventional Transmitter Architectures. In *2023 IEEE International Symposium on Circuits and Systems (ISCAS)*, pages 1–5, 2023.

[2] Mohammad Oveisi and Payam Heydari. A Study of BER and EVM Degradation in Digital Modulation Schemes Due to PLL Jitter and Communication-Link Noise. *IEEE Transactions on Circuits and Systems I: Regular Papers*, 69(8):3402–3415, 2022.

[3] Mohammad Oveisi, Seyedali Hosseinisangchi, and Payam Heydari. A Study of Out-of-Band Emission in Digital Transmitters Due to PLL Phase Noise, Circuit Non-Linearity, and Bandwidth Limitation. *IEEE Open Journal of Circuits and Systems*, pages 1–1, 2023.

[4] Behzad Razavi and Razavi Behzad. *RF microelectronics*, volume 2. Prentice hall New York, 2012.

[5] Hyejung Jung, Mark Cudak, Kevin Baum, and Vijay Nangia. Impact of out-of-band emission in ofdm and in dft-sofdm. In *VTC Spring 2009-IEEE 69th Vehicular Technology Conference*, pages 1–5. IEEE, 2009.

[6] Dietmar Rudolph. Out-of-band emissions of digital transmissions using kahn eer technique. *IEEE Transactions on Microwave Theory and Techniques*, 50(8):1979–1983, 2002.

[7] Fumihiro Hasegawa, Akihiro Okazaki, Atsushi Okamura, Damien Castelain, Cristina Ciochina-Duchesne, Loïc Brunel, and David Mottier. Novel dynamic and static methods for out-of-band power suppression in sc-ofdm. *IEEE Wireless Communications Letters*, 4(3):313–316, 2015.

[8] Jaap Van De Beek and Fredrik Berggren. Out-of-band power suppression in ofdm. *IEEE communications letters*, 12(9):609–611, 2008.

[9] Mattias Lampe and Hermann Rohling. Reducing out-of-band emissions due to nonlinearities in ofdm systems. In *1999 IEEE 49th Vehicular Technology Conference (Cat. No. 99CH36363)*, volume 3, pages 2255–2259. IEEE, 1999.

[10] Ahmed Selim and Linda Doyle. A method for reducing the out-of-band emissions for ofdm systems. In *2014 IEEE Wireless Communications and Networking Conference (WCNC)*, pages 730–734. IEEE, 2014.

[11] Xiaojing Huang, Jian A Zhang, and Y Jay Guo. Out-of-band emission reduction and a unified framework for precoded ofdm. *IEEE Communications Magazine*, 53(6):151–159, 2015.

[12] Dayoung Kim and Heung-Gyoon Ryu. Trade-off characteristic between ber performance and oob power emission in wr-ofdm system. In *2019 International Conference on Information and Communication Technology Convergence (ICTC)*, pages 846–849. IEEE, 2019.

[13] Behzad Razavi. *Design of analog CMOS integrated circuits*. MC GRAW HILL, 2017.

[14] A Bruce Carlson, Paul B Crilly, and Janet C Rutledge. *Communication systems*. 2002.

[15] Tony J Rouphael. *RF and digital signal processing for software-defined radio: a multi-standard multi-mode approach*. Newnes, 2009.

[16] David Taggart and Rajendra Kumar. Impact of phase noise on the performance of the qpsk modulated signal. In *2011 Aerospace Conference*, pages 1–10. IEEE, 2011.

[17] Ali Hajimiri and Thomas H Lee. A general theory of phase noise in electrical oscillators. *IEEE journal of solid-state circuits*, 33(2):179–194, 1998.

[18] Alper Demir, Amit Mehrotra, and Jaijeet Roychowdhury. Phase noise in oscillators: A unifying theory and numerical methods for characterisation. In *Proceedings of the 35th annual Design Automation Conference*, pages 26–31, 1998.

[19] Kenichi Okada, Ning Li, Kota Matsushita, Keigo Bunsen, Rui Murakami, Ahmed Musa, Takahiro Sato, Hiroki Asada, Naoki Takayama, Shogo Ito, et al. A 60-ghz 16qam/8psk/qpsk/bpsk direct-conversion transceiver for ieee802. 15.3 c. *IEEE Journal of Solid-State Circuits*, 46(12):2988–3004, 2011.

[20] Florent Munier, Eric Alpman, Thomas Eriksson, Arne Svensson, and Herbert Zirath. Estimation of phase noise for qpsk modulation over awgn channels. In *Proc. GigaHertz 2003 Symp*, pages 4–5, 2003.

[21] Luciano Tomba. On the effect of wiener phase noise in ofdm systems. *IEEE Transactions on communications*, 46(5):580–583, 1998.

[22] Antonios Pitarokoilis, Saif Khan Mohammed, and Erik G Larsson. Achievable rates of zf receivers in massive mimo with phase noise impairments. In *2013 Asilomar Conference on Signals, Systems and Computers*, pages 1004–1008. IEEE, 2013.

[23] Lorenzo Iotti, Andrea Mazzanti, and Francesco Svelto. Insights into phase-noise scaling in switch-coupled multi-core lc vcos for e-band adaptive modulation links. *IEEE Journal of Solid-State Circuits*, 52(7):1703–1718, 2017.

[24] M Reza Khanzadi. *Modeling and estimation of phase noise in oscillators with colored noise sources*. Chalmers Tekniska Hogskola (Sweden), 2013.

[25] David M Pozar. *Microwave and RF design of wireless systems*. John Wiley & Sons, 2000.

[26] Behzad Razavi. *Design of CMOS phase-locked loops: from circuit level to architecture level*. Cambridge University Press, 2020.

[27] John G Proakis. *Digital communications*. McGraw-Hill, Higher Education, 2008.

[28] Mozhgan Mansuri, Ali Hadiashar, and Chih-Kong Ken Yang. Methodology for on-chip adaptive jitter minimization in phase-locked loops. *IEEE Transactions on Circuits and Systems II: Analog and Digital Signal Processing*, 50(11):870–878, 2003.

[29] Mozhgan Mansuri and Chih-Kong Ken. Jitter optimization based on phase-locked loop design parameters. *IEEE Journal of Solid-State Circuits*, 37(11):1375–1382, 2002.

[30] Mozhgan Mansuri. *Low-power low-jitter on-chip clock generation*. University of California, Los Angeles, 2003.

[31] Alireza Karimi-Bidhendi, Haoran Pu, and Payam Heydari. Study and design of a fast start-up crystal oscillator using precise dithered injection and active inductance. *IEEE Journal of Solid-State Circuits*, 54(9):2543–2554, 2019.

[32] J Stott. The effects of phase noise in cofdm. *EBU technical Review*, pages 12–25, 1998.

[33] Frank Herzel, Arzu Ergintav, Johannes Borngraeber, Herman Jalli Ng, and Dietmar Kissinger. Design of a low-jitter wideband frequency synthesizer for 802.11 ad wireless ofdm systems using a frequency sixtupler. In *2017 IEEE International Symposium on Circuits and Systems (ISCAS)*, pages 1–4. IEEE, 2017.

[34] W Kester. Converting oscillator phase noise to time jitter (pdf), tech note, analog devices, retrieved oct. 10, 2019.

[35] Dongseok Shin, Hyung Seok Kim, Chuan-chang Liu, Priya Wali, Savyasaachi Keshava Murthy, and Yongping Fan. 11.5 a 23.9-to-29.4 ghz digital lc-pll with a coupled frequency doubler for wireline applications in 10nm finfet. In *2021 IEEE International Solid-State Circuits Conference (ISSCC)*, volume 64, pages 188–190. IEEE, 2021.

[36] Michel Azarian and Will Ezel. Accurately predicting pll reference spur levels due to leakage currente. *ELECTRONICS WORLD*, 119(1925):24–31, 2013.

[37] Manolis T Terrovitis and Robert G Meyer. Noise in current-commutating cmos mixers. *IEEE Journal of solid-state circuits*, 34(6):772–783, 1999.

[38] Payam Heydari. Noise analysis of passive sampling mixers using auto-and cross-correlation functions. In *2021 IEEE International Symposium on Circuits and Systems (ISCAS)*, pages 1–5. IEEE, 2021.

[39] Manolis T Terrovitis, Kenneth S Kundert, and Robert G Meyer. Cyclostationary noise in radio-frequency communication systems. *IEEE Transactions on Circuits and Systems I: Fundamental Theory and Applications*, 49(11):1666–1671, 2002.

[40] Tom AD Riley, Miles A Copeland, and Tad A Kwasniewski. Delta-sigma modulation in fractional-n frequency synthesis. *IEEE journal of solid-state circuits*, 28(5):553–559, 1993.

[41] Alan V Oppenheim, Alan S Willsky, Syed Hamid Nawab, and Jian-Jiun Ding. *Signals and systems*, volume 2. Prentice hall Upper Saddle River, NJ, 1997.

[42] Hossein Pishro-Nik. Introduction to probability, statistics, and random processes. 2016.

[43] Apostolos Georgiadis. Gain, phase imbalance, and phase noise effects on error vector magnitude. *IEEE Transactions on Vehicular Technology*, 53(2):443–449, 2004.

[44] Hooman Darabi. *Radio frequency integrated circuits and systems*. Cambridge University Press, 2015.

[45] TK Roy, MF Pervej, and M Morshed. Performance comparison of three optimized alternative pulse shaping filters with the raised cosine filter for wireless applications. In *2015 International Conference on Computer and Information Engineering (ICCIE)*, pages 9–12. IEEE, 2015.

[46] Leon W Couch, Muralidhar Kulkarni, and U Sripati Acharya. *Digital and analog communication systems*, volume 8. Citeseer, 2013.

[47] Behzad Razavi. *Design of integrated circuits for optical communications*. John Wiley & Sons, 2012.

[48] Mohammad Oveisi, Huan Wang, and Payam Heydari. A Study of a Millimeter-Wave Transmitter Architecture Realizing QAM Directly in RF Domain. *IEEE Transactions on Circuits and Systems I: Regular Papers*, 2023.

[49] Meng Wah Chia, Yonghong Zeng, and Ying-Chang Liang. Closed-form approximations to the out-of-band emission due to nonlinear power amplifier. In *2013 IEEE Wireless Communications and Networking Conference (WCNC)*, pages 4032–4036. IEEE, 2013.

[50] Charles A Desoer and Ernest S Kuh. Basic circuit theory. *(No Title)*, 1969.

[51] Arpit K Gupta and James F Buckwalter. Linearity considerations for low-evm, millimeter-wave direct-conversion modulators. *IEEE transactions on microwave theory and techniques*, 60(10):3272–3285, 2012.

[52] Adel AM Saleh. Frequency-independent and frequency-dependent nonlinear models of twt amplifiers. *IEEE Transactions on communications*, 29(11):1715–1720, 1981.

[53] Huan Wang, Hossein Mohammadnezhad, and Payam Heydari. Analysis and design of high-order qam direct-modulation transmitter for high-speed point-to-point mm-wave wireless links. *IEEE Journal of Solid-State Circuits*, 54(11):3161–3179, 2019.

[54] Michael H Perrott, Mitchell D Trott, and Charles G Sodini. A modeling approach for/spl sigma/-/spl delta/fractional-n frequency synthesizers allowing straightforward noise analysis. *IEEE Journal of Solid-State Circuits*, 37(8):1028–1038, 2002.

[55] Payam Heydari. Terahertz integrated circuits and systems for high-speed wireless communications: Challenges and design perspectives. *IEEE Open Journal of the Solid-State Circuits Society*, 1:18–36, 2021.

[56] Athanasios Papoulis and S Unnikrishna Pillai. *Probability, random variables and stochastic processes*. 2002.

Appendix A

Symmetry Analysis of Error Probabilities for Constellation Diagram Points

This appendix mathematically proves that only one eighth of the constellation diagram is sufficient for the analysis and the remaining parts are handled in the same way. The probability of error for the symbol $(I,Q)=(n,m)$ $(n>m)$ is:

$$P_e|_{(I,Q)=(n,m)} = Q\left(\frac{\sin^{-1}\frac{m+1}{\sqrt{n^2+m^2}} - \tan^{-1}\frac{m}{n}}{\sigma_{\Delta\phi}}\right) + Q\left(\frac{\tan^{-1}\frac{m}{n} - \sin^{-1}\frac{m-1}{\sqrt{n^2+m^2}}}{\sigma_{\Delta\phi}}\right) \tag{A.1}$$

The probability of error for $(I,Q)=(-n,m)$ $(n>m)$ is given by

$$\begin{aligned} P_e|_{(I,Q)=(-n,m)} &= Q\left(\frac{\pi - \sin^{-1}\frac{m-1}{\sqrt{n^2+m^2}} - \left(\pi - \tan^{-1}\frac{m}{n}\right)}{\sigma_{\Delta\phi}}\right) \\ &+ Q\left(\frac{\pi - \tan^{-1}\frac{m}{n} - \left(\pi - \sin^{-1}\frac{m+1}{\sqrt{n^2+m^2}}\right)}{\sigma_{\Delta\phi}}\right) \end{aligned} \tag{A.2}$$

A quick inspection reveals that (A.1) and (A.2) are identical. Therefore,

$$P_e|_{(I,Q)=(-n,m)} = P_e|_{(I,Q)=(n,m)} \tag{A.3}$$

Moreover, symbols $(\pm n, \pm m)$ that are mirrors of (n, m) across x- and y-axis and are located in other quadrants have the same probabilities of error, i.e., $P_e|_{(I,Q)=(\pm n,\pm m)} = P_e|_{(I,Q)=(n,m)}$. Similarly, the probability of error for $(I, Q) = (m, n)$ is given by

$$P_e|_{(I,Q)=(m,n)} = Q\left(\frac{\cos^{-1}\frac{m-1}{\sqrt{n^2+m^2}} - \tan^{-1}\frac{n}{m}}{\sigma_{\Delta\phi}}\right) + Q\left(\frac{\tan^{-1}\frac{n}{m} - \sin^{-1}\frac{m+1}{\sqrt{n^2+m^2}}}{\sigma_{\Delta\phi}}\right) \tag{A.4}$$

Due to the fact that $\tan^{-1}(n/m) = \pi/2 - \tan^{-1}(m/n)$ and $\sin^{-1} x = \pi/2 - \cos^{-1} x$, Eqs. (A.1) and (A.4) are equal, resulting in

$$P_e|_{(I,Q)=(\pm n,\pm m)} = P_e|_{(I,Q)=(\pm m,\pm n)} \tag{A.5}$$

Appendix B

Analysis of Decision Region Boundaries and Symbol Departure for Constellation Symbols

The boundaries upon which the constellation symbols leave their decision region is studied in detail in this appendix. Fig. B.1 indicates the decision region for the symbol $(I, Q) = (i, q)$, which is:

$$\begin{cases} i - 1 < I < i + 1 \\ q - 1 < Q < q + 1 \end{cases}$$

If the symbol's distance from the origin (D_S) is greater than that from the top left corner $(i - 1, q + 1)$ of its decision region ($D_{i-1,q+1}$), the symbol will fall inside the top region upon a counter-clockwise rotation and will spill into the bottom region with a clockwise rotation (the green dotted arc). Moreover, if $D_S < D_{i-1,q+1}$, the symbol leaves its decision region from the left-side with a counter-clockwise rotation, and from the right-side (the red dashed

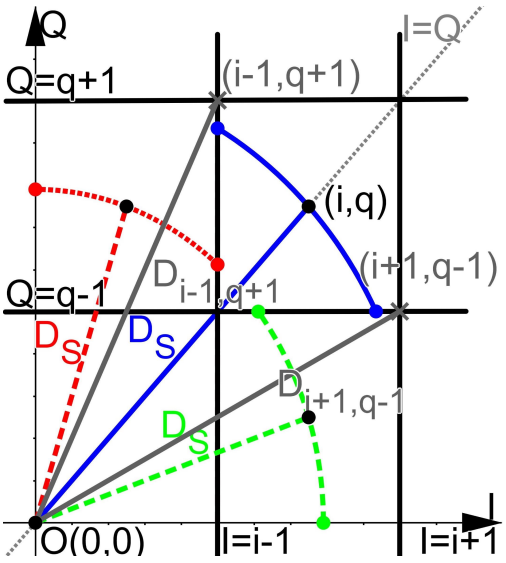

Figure B.1: Decision region for symbol (i, q).

arc) with a clockwise rotation.

The symbol's distance from the origin of the constellation plane is given by

$$D_S = \sqrt{i^2 + q^2} \tag{B.1}$$

The distance of the top left corner of the decision region $(i-1, q+1)$ from the origin is given by

$$D_{i-1,q+1} = \sqrt{i^2 + q^2 + 2\,(q - i + 1)} \tag{B.2}$$

Similarly, the distance of the bottom right corner of the decision region point $(i+1, q-1)$ from the origin is given by

$$D_{i+1,q-1} = \sqrt{i^2 + q^2 + 2\,(i - q + 1)} \tag{B.3}$$

Therefore,

$$D_S > D_{i-1,q+1} \iff i - q > 1 \tag{B.4}$$

$$D_S < D_{i-1,q+1} \iff i - q < 1 \tag{B.5}$$

$$D_S > D_{i+1,q-1} \iff i - q < -1 \tag{B.6}$$

$$D_S < D_{i+1,q-1} \iff i - q > -1 \tag{B.7}$$

It is observed that for diagonal symbols (i.e., $i = q$), (B.5) and (B.7) hold. For symbols that are to the right of the diagonal symbols (i.e., $i - q \geqslant 2$), (B.4) and (B.7) hold. Finally, for symbols that are to the left of the diagonal symbols (i.e., $i - q \leqslant -2$), (B.5) and (B.6) hold. Therefore, the diagonal symbols subject to PLL jitter leave their decision region from the left side and bottom boundaries. The ones located on the right side of the diagonal symbols leave their decision region from the top and bottom boundaries. Finally, those on the left side of the diagonal symbols leave their decision region from the left and right sides.

Appendix C

Power Spectral Density Analysis for the Product of Independent Processes

This appendix provides the PSD of a multiplication of two independent processes. It is widely known that the PSD of a random process is the Fourier transform of its autocorrelation function[27, 56]. Assuming $z(t) = x(t) \times y(t)$, PSD of $z(t)$ (i.e., $S_Z(f)$) can be obtained by calculating its autocorrelation function. For two wide-sense stationary (WSS) processes, we have

$$R_Z(\tau) = \mathbb{E}[z(t)z(t+\tau)] = \mathbb{E}[x(t)y(t)x(t+\tau)y(t+\tau)] \tag{C.1}$$

where $R_Z(\tau)$ is the autocorrelation function of random process Z. In the case where X and Y are independent, Eq. (C.1) can be simplified to:

$$R_Z(\tau) = \mathbb{E}[x(t)x(t+\tau)] \times \mathbb{E}[y(t)y(t+\tau)] = R_X(\tau) \times R_Y(\tau) \tag{C.2}$$

Taking the Fourier transform of Eq. (C.2) results in:

$$S_Z(f) = S_X(f) * S_Y(f) \tag{C.3}$$

Appendix D

Mathematical Derivations for EVM Due to Nonlinearity in Conventional 4^MQAM Transmitters

The details and the mathematical derivations of the conventional 4^MQAM transmitter's EVM is presented in this section. The average rotation angle of the constellation diagram's symbols is calculated to be

$$\theta_{avg} = \frac{1}{4^{M-1}} \sum_{n\in\text{odd}}^{2^M-1} \sum_{m\in\text{odd}}^{2^M-1} \frac{\alpha_2 a_u^2 \left(n^2+m^2\right)}{1+\beta_2 a_u^2 \left(n^2+m^2\right)} \tag{D.1}$$

Using Eqs. (6.13)-(6.15), d is readily calculated:

$$d = \sqrt{\frac{6}{\left(4^M-1\right)\times 4^M} \sum_{n\in\text{odd}}^{2^M-1} \sum_{m\in\text{odd}}^{2^M-1} \frac{\alpha_1^2 a_u^2 \left(n^2+m^2\right)}{\left[1+\beta_1 a_u^2 \left(n^2+m^2\right)\right]^2}} \tag{D.2}$$

Moreover, $d_{n,m}$ is defined to be $d_{n,m} = d\sqrt{n^2+m^2}$. Additionally, $\psi_{n,m} = \theta_{n,m} - \theta_{avg}$ is the effective phase difference between the transmitted $(I,Q) = (n,m)$ symbol and its corre-

sponding reference constellation point, and is derived, as:

$$\begin{aligned}\psi_{n,m} = & \frac{\alpha_2 a_u^2 \left(n^2+m^2\right)}{1+\beta_2 a_u^2 \left(n^2+m^2\right)} \\ & - \frac{1}{4^{M-1}} \sum_{n\in\text{odd}}^{2^M-1} \sum_{m\in\text{odd}}^{2^M-1} \frac{\alpha_2 a_u^2 \left(n^2+m^2\right)}{1+\beta_2 a_u^2 \left(n^2+m^2\right)}\end{aligned} \tag{D.3}$$

These derivations are used throughout the text to calculate the EVM in the conventional 4^MQAM transmitter.